nature portfolio

Peer Review File

Continuously graded-doped SnO2 for efficient n-i-p perovskite solar cells

Corresponding Author: Professor Mingjian Yuan

Any redactions in this file are there to maintain patient confidentiality, the confidentiality of unpublished data, or to remove third-party material.

Parts of this Peer Review File have been redacted as indicated to remove third-party material.

Attachments originally included by the reviewers as part of their assessment can be found at the end of this file.

Version 0:

Reviewer comments:

Referee #1

(Remarks to the Author)
This manuscript reports a record-breaking certified power conversion efficiency (PCE) of 27.17% in n-i-p perovskite solar cells (PSCs) by employing a 'Ligand-Competitive Binding (LCB)' strategy to create a continuously graded-doped (CGD) SnO_2 layer. The methodology is rigorous, and the use of advanced depth-profiling (TOF-SIMS, HAXPES) and simulations (DFT, AIMD) provides a high level of confidence in the structural characterization.
While the results are of immediate interest to the global photovoltaics community due to the unprecedented efficiency, there are several fundamental aspects regarding the underlying mechanisms and methodology that require further clarification. I would like the authors to address the following points before publication.
1. Please elaborate on the specific physical or optoelectronic advantages that a "continuous gradient" offers over an optimized "discrete bilayer".
2. Regarding the long-term stability and ligand dynamics, many organic ligands are known to migrate or desorb under thermal and environmental stress. What prevents the PA and SA ligands from diffusing within the SnO_2 matrix or into the perovskite layer during operation? To further substantiate the robustness of this LCB-SnO_2 architecture, I highly recommend the authors to provide additional stability data under ISOS-D-3 (Damp Heat: 85°C and 85% RH) conditions, as this is a crucial metric for evaluating the reliability of interfacial engineering in PSCs.
3. Is the 27.17% efficiency truly a result of the continuously graded doping profile, or is it primarily driven by the simple chemical passivation of the SnO_2 surface by the ligands? Please provide a more rigorous control experiment or physical justification to decouple the electronic effects of 'graded doping' from 'interface passivation'.
4. The LCB strategy involves acidic organic ligands (SA and PA) that remain at the SnO_2 surface. How do these residual ligands influence the initial nucleation and grain growth of the overlying perovskite layer? Specifically, is there any evidence of side reactions between the sulfonic/phosphonic acid groups and the lead ions (Pb^{2+}) that might form an insulating intermediate layer (e.g., $PbSO_4$ or Pb-PA complexes)?
5. The reported Jsc of 26.48 mA/cm^2 is exceptionally high. Could the authors clarify the specific mechanisms by which the LCB-SnO_2 strategy contributes to such an enhanced current density?
6. The certified steady-state efficiency of 27.17% reported in this work is arguably the highest for n-i-p perovskite solar cells and even exceeds the current world record for perovskite cells on the NREL Best Research-Cell Efficiency Chart. Could the authors clarify why this result has not yet been updated on the NREL chart? Furthermore, do the authors have plans to submit this cell for an official NREL or ISFH record listing to verify its standing as a new global benchmark?

Referee #2

(Remarks to the Author)
SnO2 serves as an electron-transport layer in conventional (n-i-p) perovskite solar cells, where its interfacial properties directly govern device efficiency and long-term stability. Despite its importance, optimizing SnO2 remains a major challenge due to the intricate surface chemistry of its nanocrystals, which often introduces trap states and energy-level misalignment

that compromise performance. The graded SnO2 architecture reported by Yuan et al. offers an effective means to this bottleneck by enabling systematic modulation of surface defects and energy landscapes. This strategic approach delivers substantial gains in power-conversion efficiency while enhancing operational stability, representing a significant advance in the field. The work is suitable for publication in Nature after the authors address the following concerns.
1. As a typical HTL, Sprio-OMeTAD generally shows an electron mobility of less than 10-4 cm2 V-1 S-1, usually on the order of 10-7 to 10-5 cm2 V-1 S-1. This is inconsistent with the measured value of 2.8 × 10-3 cm2 V-1 S-1 shown in Supplementary Fig. 6. In addition, is it appropriate to compare the electron mobility of TGA-SnO2 and Sprio-OMeTAD to state that there is an imbalance in the electron-hole extraction for TGA-SnO2-based device, given that the main function of Sprio-OMeTAD is to block the electrons rather than transport them?
2. The of oxygen vacancies (Vo) concentration plays an important role in the properties of SnO2 layer. The authors have conducted a specific analysis of the minimum electrostatic potential (φmin) and the Sn2+/Sn4+ ratio for different ligands, including TGA, MA, PA and SA (Fig. 1d and 1g). However, it appears that there is no clear relationship between φmin, the Sn2+/Sn4+ ratio and Vo in the manuscript. The authors should clarify and comment on this point.
3. According to the trend in the minimum electrostatic potential (φmin) of φmin MA < φmin PA < φmin SA (Line 144, Page 7; Fig. 1d and Supplementary Fig. 11), the authors predict that the SA-capped SnO2 NPs would yield the highest Vo concentration and the best band alignment at the buried interface. Does there exist any bidentate ligand with a higher φmin? Or can such ligands be synthesized?
4. What is quasi-layer by layer (quasi-LBL)?
5. How do the authors precisely control and monitor the hydrolysis of DMPA? This may be a key factor for the reproducibility of the manuscript.
6. In general, for the SnCl2-based CBD process, the solution is typically acidic, with a pH value of around 1–2. The authors also mention in Supplementary Note 3 that a strongly acidic environment induces deprotonation of carboxyl groups, driving electrostatic adsorption onto the FTO substrate. However, in Fig. 2a, the chemical equation show that the reverse reaction of DMPA hydrolysis may occur under H+-rich conditions, suggesting that DMPA is more likely to remain stable in an acidic environment. Therefore, is it possible that DMPA does not fully undergo hydrolysis under these conditions? If so, the final ETL structure may be a SA-SnO2/ DMPA-SnO2 gradient, rather than the proposed SA-SnO2 (n+)/ PA-SnO2 (n) gradient. The authors should provide compositional identification of the ETL intermediate prior to annealing at 170 °C to clarify this issue.
7. Is it possible to generate a graded structure by gradually introducing PA ligands into a solution that already contains SA ligands at an intermediate stage during a 4-hour chemical bath deposition process?
8. In the PCE certification report (Supplementary Fig. 23), the discrepancy in FF between the forward and reverse J–V scans (80.79% vs 86.48%) suggests pronounced hysteresis. Could this originate from residual ligands in the graded SnO2 layer, or from other factors?
9. It would be helpful for the authors to provide PL results to confirm the 1.51 eV bandgap of the perovskite, thereby strengthening the basis for the reported Voc loss of 295 mV.
10. Although the device performance for n-i-n perovskite solar cells is impressive, but thermal stability and thermal-recyling assessements are needed to be done in the revised manuscript.
11. I appreciate the SI writing style that combines the Supplementary Notes and Supplementary Figures, which greatly facilitates understanding. For even smoother reading, it may be helpful if the authors could consider aligning the numbering of figures and supplementary figures with the order of their appearance in the corresponding text.

Minor mistakes:
1. Line 250, Page 14: A Chinese comma symbol (“ ， ”) is used.

Referee #3

(Remarks to the Author)
A. In this report, the authors describe the utilization of a graded SnO2 bandgap that achieves a near 10% enhancement in the efficiency of a perovskite solar cell. The authors identify a defect within the SnO2 electron transport layer that hinders charge transfer and directly impacts the voltage and FF. Through simulations, they attribute this to oxygen vacancies that act as shallow donors. The authors surmise that this is due to the CBD deposition of the SnO2 nanoparticles and propose that this can be resolved using a straightforward ligand strategy. However, to accomplish this, they employ a rather unique chemical strategy to manage the ligand. As a result, they are able to utilize the CBD process to create a graded bandgap. With this in place, they are able to demonstrate an improved efficiency for a device on a non-uniform surface. This paper is well-written and the narrative manages the reader’s interest and builds a solid story. From the scientific merits of the work, it is solid.
B. The proposed ligands and use of ligands to achieve highly uniform results with SnO2 have been studied before, as described by the authors. However, the use of the dual ligand strategy to achieve a graded bandgap using the CBD strategy is novel.
C. The data quality and the utilization of experiments and simulations to identify the issues associated with the buried interface, along with the validation of the proposed solution’s effectiveness, are present.
D. The authors employ a sufficient number of devices to conduct a robust statistical analysis.
E. The conclusions are supported by the data.
F. The primary concern from this reviewer’s perspective is the need for an improved ETL for a non-uniform surface and of course how this process is expanded for high throughput production.
1- The authors’ motivation in the introduction is that the utilization of textured surfaces for light management has enhanced the power conversion efficiency (PCE) of photovoltaic cells. Textured surfaces are often incorporated into silicon solar cells and contribute to improved PCE. Consequently, the development of chemistries and processes aimed at achieving higher efficiencies is driven by the tandem architecture, which favors the p-i-n structure.

a. Thus it would be helpful if the authors address this issue, ie, can this process be adapted to perovskite/tandems or what is the opportunity for these devices.
b. On line 82 page 4, the authors describe the fabrication of SnO2 on a textured FTO, but do not mention the RMS of the textured FTO. The amount texture as seen in Fig 2g, and SI 16 shows a pyramid like structure about 100-200 nm tall. And these do not seem to be distributed over the larger area. So, the RMS is probably on the order of 10's of nm. In contrast a textured surface for a silicon solar cell uses pyramids of several microns and optimized texturing for perovskite/silicon tandems the pyramids are ~0.5 microns. Thus, the authors are encouraged to put a bit more context on the texturing.
c. It would also be helpful to the reader if the authors discussed the importance of the RMS values on their process. Is there a point that the CBD and/or grade bandgap breaks down.
2- The chemical bath deposition process is a scalable process and can result in large area uniform films (1 m2), and has been demonstrated for CIGS devices. However, trhe reality is that the process in inherently slow, as is detailed within this manuscript. Therefore it would aid the reader if the authors would provide a prospective of the utility of the proposed chemistry/process.
G. References are appropriate.
H. The manuscript is well-written, and the story has a logical narrative. The authors are encouraged to provide context for the scientific discussion in the broader implications of this study, as outlined above.

Version 1:

Reviewer comments:

Referee #1

(Remarks to the Author)
I have carefully read the rebuttal letter and reviewed the revised manuscript. The authors have adequately addressed the comments raised in the previous round of review, and the manuscript has been significantly improved.

In my opinion, the authors have satisfactorily responded to the reviewers' comments, and I believe the manuscript is now suitable for publication in its current form.

I therefore recommend acceptance of this manuscript.

Referee #2

(Remarks to the Author)
The authors have carefully addressed the previous comments with additional experiments and analyses. The manuscript has been significantly strengthened, and the main conclusions are now well supported.I would recommend publication in nature after addressing minor revisions.
I have two minor points that could further clarify the interpretation:
1. The authors attribute the observed hysteresis primarily to the measurement-protocol dependence inherent to mixed ionic-electronic perovskites, which is reasonable. However, while scan conditions indeed affect hysteresis, this does not fully exclude potential interfacial contributions from the ETL. It would therefore be helpful if the authors could provide more direct evidence (e.g., comparison with control ETLs) to better isolate interfacial effects from measurement-induced hysteresis.
2. The added stability data are valuable. As PTAA is used in these tests, it would be useful to clarify the relative contributions of the graded SnO2 ETL and the HTL replacement to the improved stability. Specifically, to what extent the observed stability enhancement can be attributed to the graded SnO2 architecture itself, rather than to the use of a more thermally stable HTL.

Referee #3

(Remarks to the Author)
The scalability and and adaptability to tandems were this reviewers primary concerns, and neither was overtly discussed in the revision to the main manuscript, all of the details are left to the SI, and not referenced in the main manuscript. The authors have answered the question raised, nut the reader may not know the results of this because they are not pointed to the discussion in the SI in the main manuscript. I would ask that the authors please include some discussion in the main text that will point the reader to the more detailed discussion in the SI describing the implications for tandems and scaling . This will aid any reader who is eager to try this process.

Referee #1:

This manuscript reports a record-breaking certified power conversion efficiency (PCE) of 27.17% in n-i-p perovskite solar cells (PSCs) by employing a 'Ligand-Competitive Binding (LCB)' strategy to create a continuously graded-doped (CGD) SnO_2 layer. The methodology is rigorous, and the use of advanced depth-profiling (TOF-SIMS, HAXPES) and simulations (DFT, AIMD) provides a high level of confidence in the structural characterization. While the results are of immediate interest to the global photovoltaics community due to the unprecedented efficiency, there are several fundamental aspects regarding the underlying mechanisms and methodology that require further clarification. I would like the authors to address the following points before publication.

Response: We really appreciate the reviewer's very instructive suggestions. To address all the concerns raised by the reviewer, we immediately returned to the lab to perform additional experimental and theoretical studies. With the help of the editors and reviewers, we have now fully addressed all issues raised by reviewers, which greatly deepened our findings. We believe the quality of the manuscript has been substantially reinforced, thanks to the reviewer's great helps.

Comment 1. Please elaborate on the specific physical or optoelectronic advantages that a "continuous gradient" offers over an optimized "discrete bilayer".

Response: Thanks for the reviewer's insightful comment. To clarify the advantages of the continuously graded doping (CGD) structure over an optimized discrete bilayer, we have conducted additional experiments and device simulations. The results consistently demonstrated that the CGD SnO_2 electron transport layer (ETL) yielded superior photovoltaic performance, primarily due to enhanced electron extraction and suppressed interfacial nonradiative recombination. The detailed evidence was provided below.

1) We first constructed a discrete bilayer ETL by sequential deposition of SA-SnO_2 (0.3 mM SA-ligand for 3 h) and PA-SnO_2 (0.15 mM PA-ligand for 3 h), according to the deposition time-thickness profile (**Supplementary Fig. 9**, **Fig S1a**). The process yielded a total film thickness of ~43 nm, which was comparable to that of the CGD ETL. Cross-sectional SEM and surface imaging confirmed that the bilayer ETL was uniform and compact, analogous to the CGD counterpart (**Fig S1b**, **c**). TOF-SIMS analysis verified the intended SA-SnO_2/PA-SnO_2 bilayer structure, with the SO_3^- signal localized at the bottom and the PO_2^- signal at the top (**Fig. S2**).

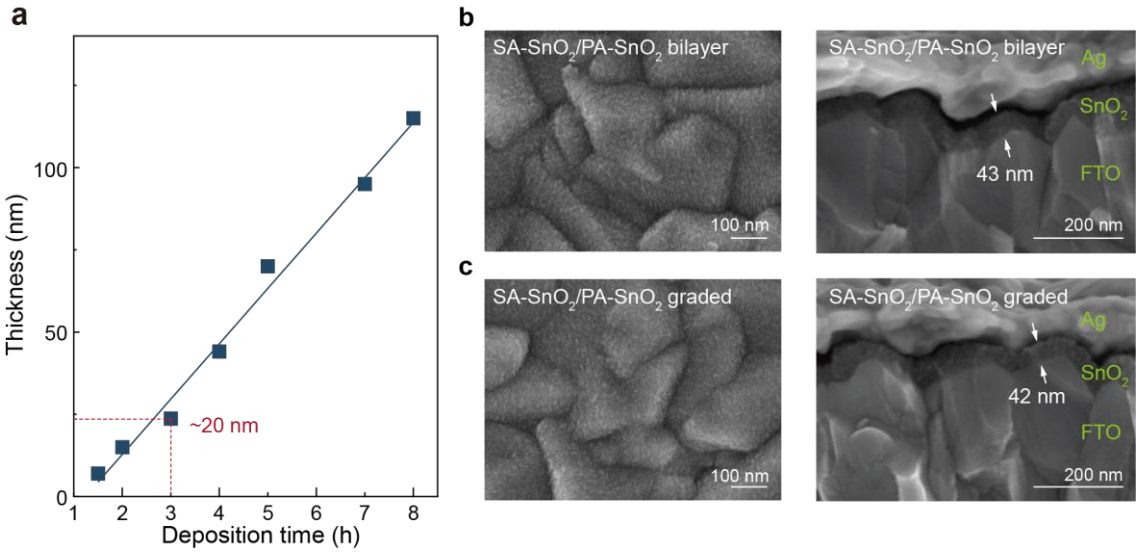

Fig. S1. *(**a**) SnO_2 films thickness versus deposition time profile. SEM and cross-sectional SEM images of SA-SnO_2/PA-SnO_2 bilayer film (**b**) and SA-SnO_2/PA-SnO_2 graded film (**c**).*

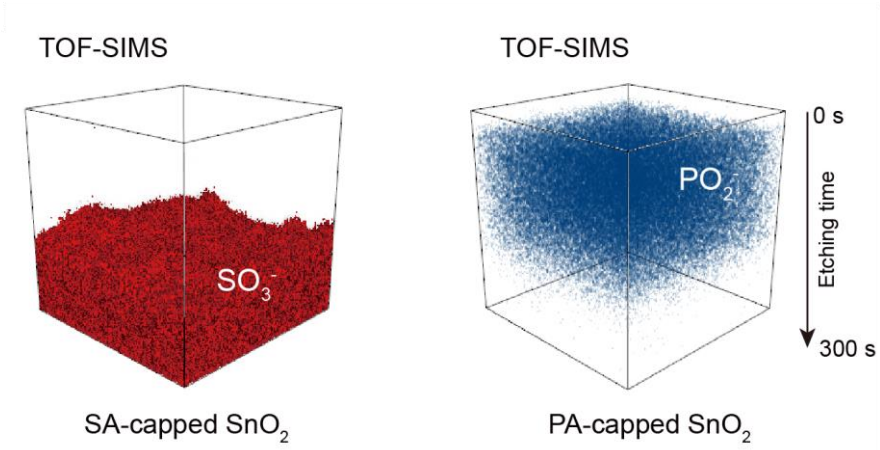

Fig. S2. *TOF-SIMS 3D mapping for PO_2^- from PA ligand and SO_3^- from SA ligand.*

We then fabricated photovoltaic devices using these two types of SnO_2 ETLs, and evaluated the device performance. As shown in **Fig. S3**, the CGD ETL device delivered higher power conversion performance (PCE) of 27.64% in reverse scan compared to 26.95% for the bilayer ETL devices, indicating clear performance advantage for the graded architecture.

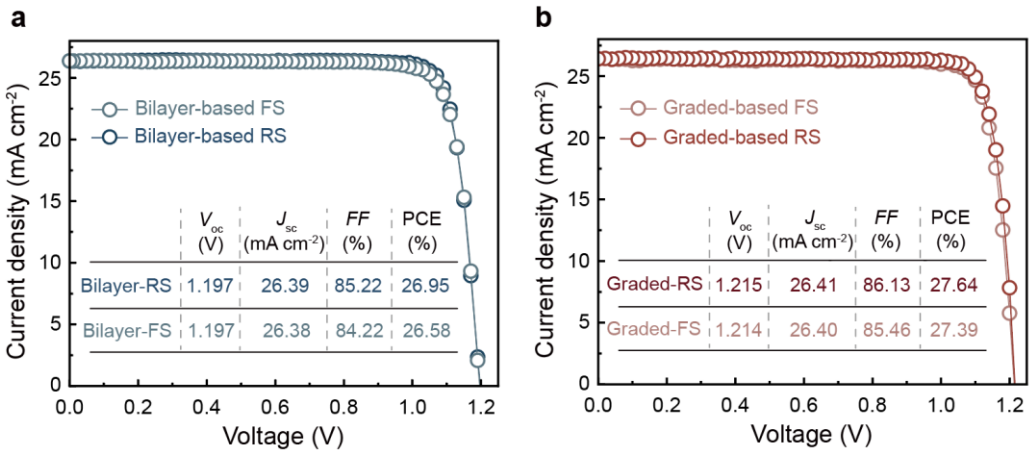

Fig. S3. *J-V curves for n-i-p devices based on bilayer (**a**) and graded SnO_2 ETL (**b**), respectively.*

2) To in-depth understand the mechanism, we performed time-resolved photoluminescence (TRPL) measurements to examine the carrier dynamics at the interface. TRPL data revealed faster electron extraction at the CGD ETL/perovskite interface. The differential lifetime τ exhibited a more rapid initial rise for the graded structure (**Figs. S4a**, **b**).

To further quantify the charge transfer dynamics, the electron-transfer rate (k_{ET}) and extraction efficiency (η_{ET}) were calculated for both interfaces according to **Equations 1-3** (summarized in **Table 1**). The analysis yielded an electron-transfer rate (k_{ET}) of 4.18×10^7 s^{-1} and extraction efficiency (η_{ET}) of 99.19% for the graded interface, outperforming the bilayer interface (3.69×10^7 s^{-1} and 99.13%; Table 1). These enhancements were attributed to improved field-driven charge extraction, which effectively reduced carrier accumulation and nonradiative recombination at the buried interface. Consistently, higher PLQY and QFLS values were observed for the graded ETL/perovskite stack, approaching those of the neat perovskite film (**Figs. S4c, d**).

$$k_{ET} = \frac{1}{\tau_{ave}} \quad (1)$$

$$\frac{1}{\tau_{Heterojunction}} = \frac{1}{\tau_{PVSK}} + \frac{1}{\tau_{ETL/PVSK}} \quad (2)$$

$$\eta_{ET} = \frac{\tau_{Heterojunction}}{\tau_{ETL}} \quad (3)$$

where $\tau_{Heterojunction}$, τ_{PVSK} and $\tau_{ETL/PVSK}$ represent the decay lifetime of heterojunction, neat perovskite, and ETL/perovskite, respectively.

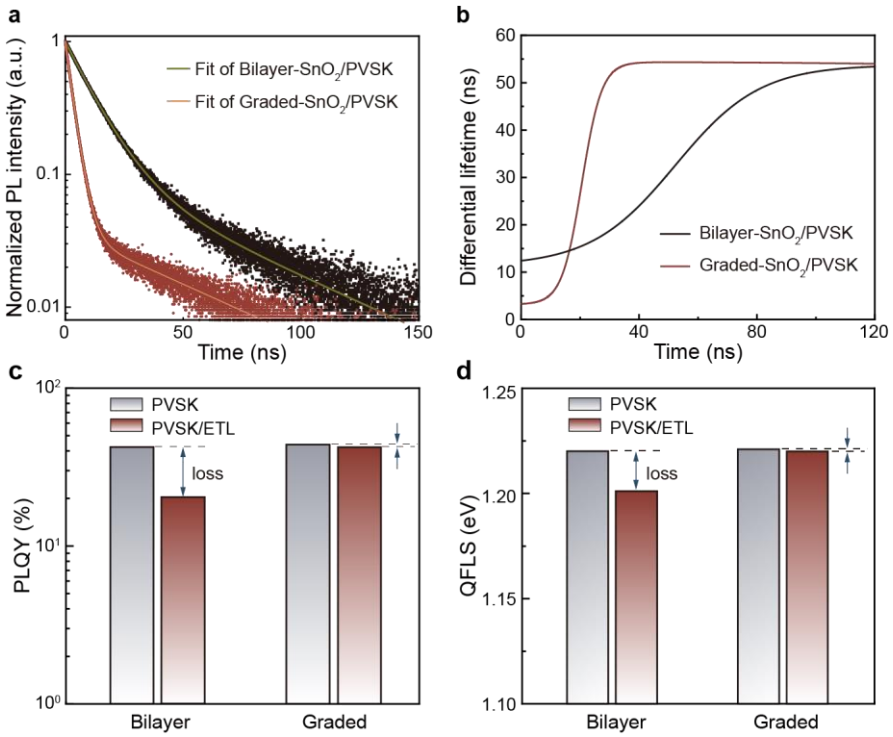

Fig. S4. *TRPL spectra (**a**) and differential lifetimes (**b**) of bilayer-SnO_2/perovskite and graded-SnO_2/perovskite stacks. PLQY spectra (**c**) and corresponding QFLS (**d**) for perovskite stacked with bilayer-SnO_2 and graded-SnO_2 ETLs.*

Table 1. TRPL fitting parameters for control-SnO_2/perovskite, bilayer-SnO_2/perovskite and CGD-SnO_2/perovskite stacks.

Sample	τ_{ave} (ns)	k_{ET} (s^{-1})	η (%)
Perovskite	3,090.1	-	-
Control-SnO_2/perovskite	86.7	1.15×10^7	97.14
Bilayer-SnO_2/perovskite	27.1	3.69×10^7	99.13
Continuously graded-SnO_2/perovskite	23.9	4.18×10^7	99.19

3) We further performed solar cell capacitance simulator (SCAPS-1D) simulations (details described in **Supplementary Table 2**) to evaluate device performance for the discrete bilayer and CGD ETL structure. As shown in **Fig. S5**, devices with a CGD ETL exhibited a notably higher open-circuit voltage (V_{oc}) than their bilayer counterparts, indicating suppressed recombination. The simulated PCE of the graded device aligned well with experimental results, reinforcing the conclusion that the graded structure offers distinct optoelectronic benefits over a discrete bilayer.

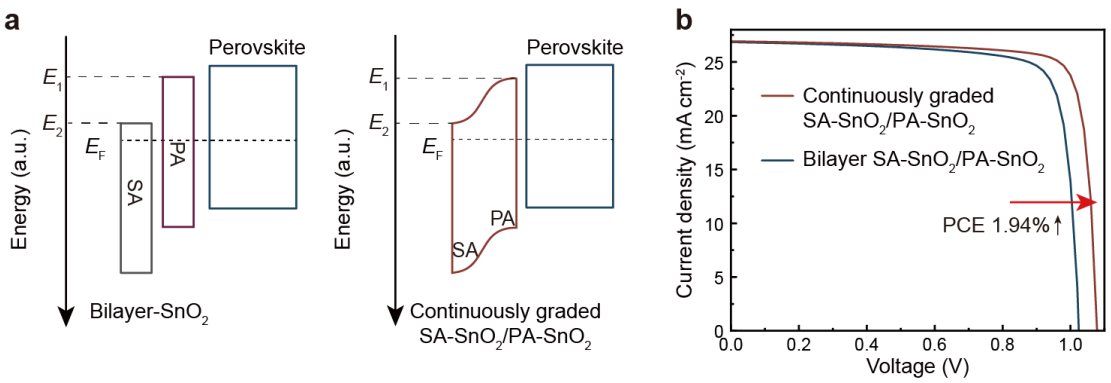

Fig. S5. *(**a**) Schematic diagrams of devices stacks based on bilayer or graded SnO_2 ETL. (**b**) Simulated J-V curves based on bilayer or graded SnO_2 ETL.*

In summary, both experimental and theoretical evidence confirmed that the continuously graded SnO_2 ETL enhanced device performance by promoting efficient electron extraction and minimizing interfacial recombination, advantages not achievable with an optimized discrete bilayer. We thank the reviewer for prompting this deeper investigation, which has substantially strengthened the manuscript.

Action: We have now confirmed that the continuously graded SnO_2 ETL exhibited notable advantages over an optimized bilayer structure, as demonstrated by both experiments and simulations (**Supplementary Note 5** and **Supplementary Note 10**, **Pages 40-42**). In particular, TRPL measurements were employed to probe carrier dynamics at the buried interface, revealing enhanced electron extraction in the graded device—an improvement that directly contributes to the enhanced device performance. Detailed discussions have been incorporated into the revised manuscript (**Line 190**, **Page 10**; **Line 287**, **Page 16**; **Line 322**, **Page 18**), and the fabrication details of the bilayer ETL have been added to the Methods section (**Line 460**, **Page 26**).

Comment 2. Regarding the long-term stability and ligand dynamics, many organic ligands are known to migrate or desorb under thermal and environmental stress. What prevents the PA and SA ligands from diffusing within the SnO_2 matrix or into the perovskite layer during operation? To further substantiate the robustness of this LCB-SnO_2 architecture, I highly recommend the authors to provide additional stability data under ISOS-D-3 (Damp Heat: 85°C and 85% RH) conditions, as this is a crucial metric for evaluating the reliability of interfacial engineering in PSCs.

Response: We thank the reviewer for raising this important point regarding the long-term stability and potential ligand migration. To address whether the PA and SA ligands may diffuse within the SnO_2 matrix or migrate into the perovskite layer during operation, we have

performed additional AIMD simulations and TOF-SIMS measurements on aged samples. Furthermore, following the reviewer's recommendation, we have conducted device stability tests under ISOS-D-3 conditions (85 °C and 85% RH). In particular, the devices retained ~90% of initial efficiency after ~950 h of continuous operation, confirming the robustness of the LCB-SnO_2. The results collectively demonstrated that the LCB-SnO_2 architecture exhibited robust binding and excellent operational stability. The detailed experiments and discussion were provided below.

1) To directly assess whether ligand desorption or interlayer diffusion occurs under operational conditions, we performed TOF-SIMS measurements on encapsulated graded-SnO_2/perovskite films subjected to aging at 85 °C and 85% RH under continuous illumination for up to 500 h. As shown in **Fig. S6**, the aged sample (500 h) exhibited no obvious changes compared to the fresh film. Critically, no PO_2^- or SO_3^- signals were detectable within the perovskite layer after aging, and their graded distribution within the SnO_2 ETL was fully preserved. These results confirmed that the ligands remain robustly bound to SnO_2, with no desorption or interlayer diffusion.

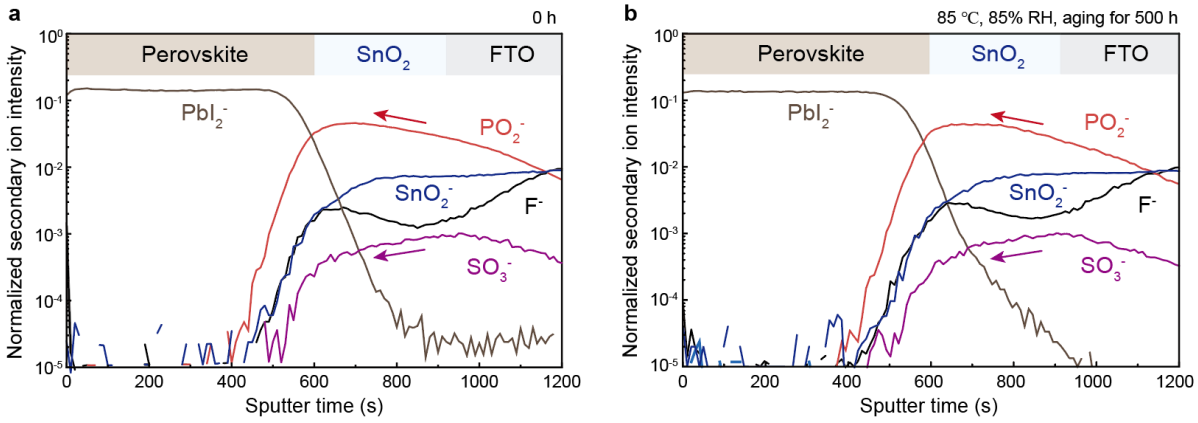

Fig. S6. *TOF-SIMS depth profiles of SnO_2/perovskite film with aging treatments for 0 h (**a**) and 500 h (**b**) under 85 °C and 85% RH, respectively.*

To gain mechanistic insight, we further conducted *ab initio* molecular dynamics (AIMD) simulations for ligand-bound SnO_2 at 358 K (85 °C). The simulations were run for 8 ps to ensure thermodynamic equilibration and to capture the dynamic behavior of ligand-surface interactions under elevated temperature. As shown in **Fig. S7**, both SA and PA ligands remained firmly anchored to the SnO_2 surface throughout the simulation trajectory after equilibration, with no desorption events observed. The AIMD results provided atomic-scale evidence that the strong ligand-substrate binding confers high intrinsic resistance to thermal and humid stress, consistent with the TOF-SIMS observations.

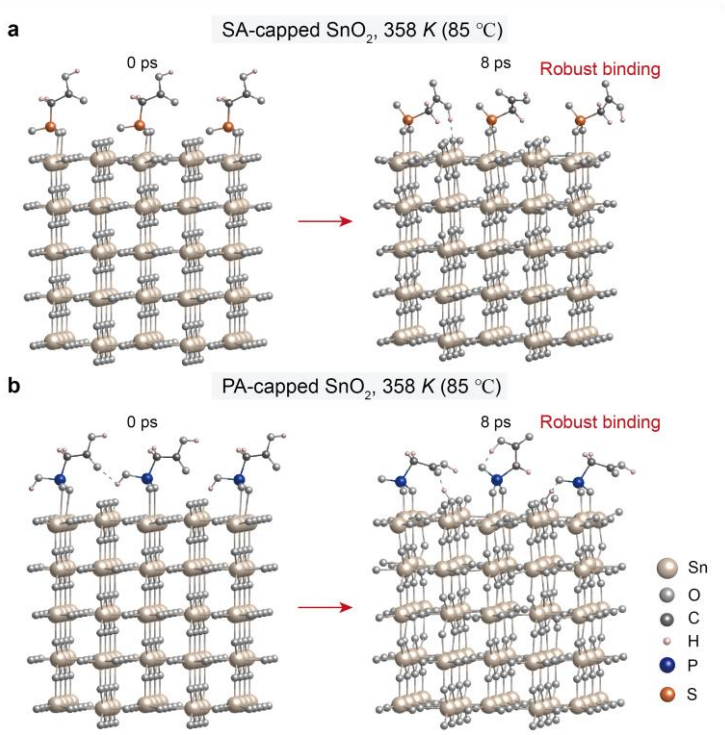

Fig. S7. *AIMD simulations of ligands binding for SA (**a**) and PA (**b**) ligands under 358 K (85 ℃).*

2) Following the reviewer's suggestion, we rigorously evaluated device stability under damp-heat conditions following the ISOS-D-3 protocol (85 °C and 85% RH). To precisely track the stability of the SnO_2 ETL without interference from potential degradation of the hole transport layer, we replaced the conventional Spiro-OMeTAD with poly[bis(4-phenyl) (2,4,6-trimethylphenyl)amine] (PTAA), which is known to exhibit superior thermal stability (*Nat. Energy* 2025, **10**, 774; *Nat. Photon.* 2025, **19**, 701; *Science* 2022, **377**, 531 et al.). As shown in **Fig. S8**, the LCB-SnO_2-based device retained ~90% of its initial efficiency after ~956 h of continuous tracking under ISOS-D-3 conditions. This stability performance was comparable to the best reported values for n-i-p perovskite solar cells to date (**Table 2**), further confirming the robustness of the LCB- SnO_2 architecture.

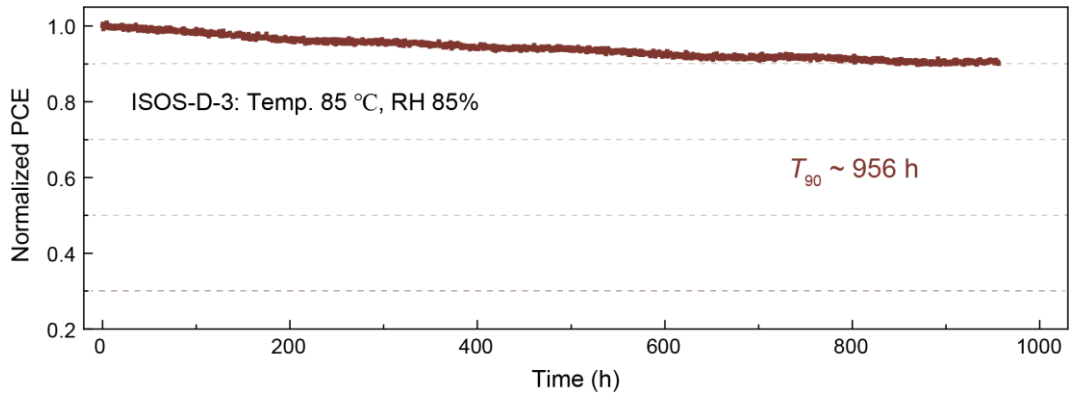

Fig. S8. *Damp-heat stability of the continuously graded-doped SnO_2-based encapsulated PSCs under ISOS-D-3 protocols (85 ℃, 85% relative humidity).*

Table 2. Summary of the reported operating stability of n-i-p PSCs under damp-heat conditions (ISOS-D-3 conditions).

ISOS protocol	Relative Humidity	Temperature	Lifetime	Ref.
ISOS-D-3	**~85%**	**85 °C**	**T_{90} = 956 h**	**This work**
ISOS-D-3	~85%	85 °C	T_{86} = 900 h	*Nat. Energy* 2025, 10, 774
ISOS-D-3	~85%	85 °C	T_{92} = 600 h	*Science* 2024, 384, 878

Action: We have now confirmed by additional TOF-SIMS measurements on aged films (85 °C, 85% RH for 500 h) and AIMD simulations, the robust binding between ligands and SnO_2 effectively prevents ligand diffusion during operation. These data have been provided in **Supplementary Note 12**, **Pages 49-50**. Furthermore, following the reviewer's suggestion, we have included device stability measurements under the ISOS-D-3 protocol (85 °C, 85% RH) in **Supplementary Fig. 51** and **Supplementary Table 6**, where the devices retain ~90% of their initial efficiency after 956 h. The corresponding experimental details and discussions have been incorporated into the revised manuscript (**Line 337**, **Page 19**).

Comment 3. Is the 27.17% efficiency truly a result of the continuously graded doping profile, or is it primarily driven by the simple chemical passivation of the SnO_2 surface by the ligands? Please provide a more rigorous control experiment or physical justification to decouple the electronic effects of 'graded doping' from 'interface passivation'.

Response: We thank the reviewer for this insightful comment. To clarify whether the record efficiency arises from the graded doping structure itself or merely from ligand passivation at the SnO_2 surface, we have conducted a series of control experiments using SnO_2 ETLs capped with different ligands or mixed ligands. The results unequivocally demonstrated that the continuously graded doping architecture is the key enabler of the enhanced performance, beyond any passivation effect. The detailed experimental evidence was provided below.

1) As described in the manuscript, the SnO_2 ETL fabricated *via* chemical bath deposition consists of ligand-capped nanoparticles, a feature also presents in conventional methods using additives such as TGA (*Nature* **2021**, 590, 587). In principle, the presence of these ligands can impart a surface passivation effect. To disentangle this passivation effect from the graded doping effect, we designed two control systems that isolate the influence of the graded distribution while preserving the ligand chemistry at the interface or within the bulk.

Pure PA-capped SnO_2 (no graded doping, but identical interfacial chemistry): This ETL shares the same PA ligand termination at the perovskite interface as the graded ETL, ensuring identical chemical passivation at the contact, but lacks the graded doping profile (**Fig. S9b**).

Mixed PA/SA-capped SnO_2 (no graded doping, but identical bulk ligand composition): By introducing PA and SA ligands at a 1:4 molar ratio during synthesis, we obtained SnO_2 nanoparticles capped with both ligands in an approximately 1:1 ratio (confirmed by XPS, **Fig. S10**). This ETL mimics the bulk ligand environment of the graded structure, but also without a doping profile (**Fig. S9c**).

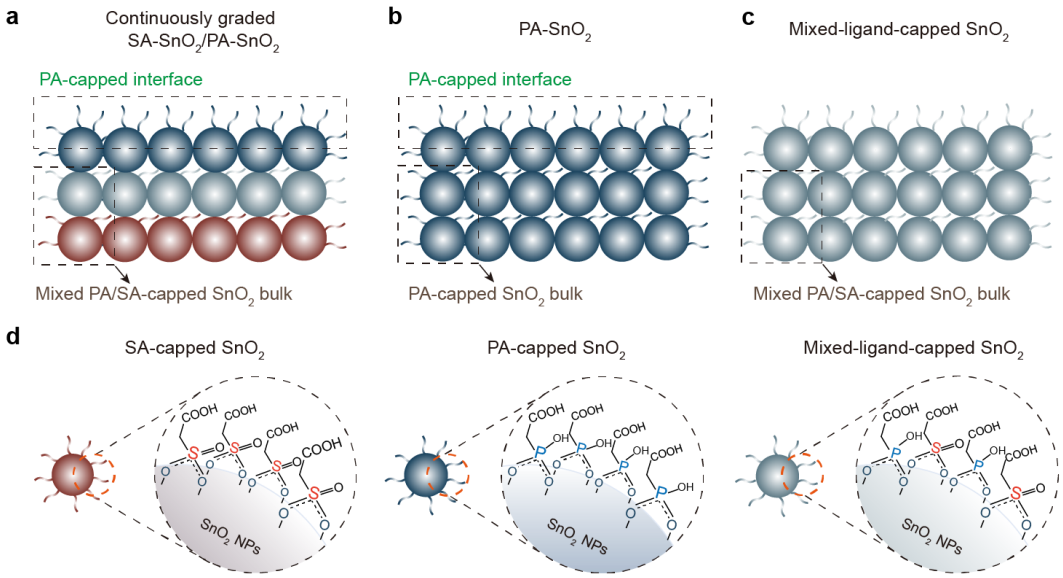

Fig. S9. *(**a**, **b**, **c**) Schematic diagrams of SnO_2 films with different ligands capping at the interface or within the bulk. (**d**) Schematic diagrams of different ligands capped SnO_2 nanoparticles.*

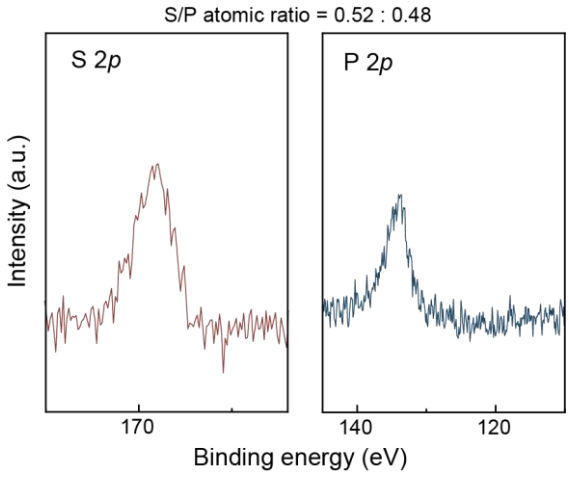

Fig. S10. *XPS spectra of P 2p and S 2p signal for mixed-ligand-capped SnO_2.*

2) Then we compared device performance to verify whether the continuously graded structure can outperform the homogeneous ligand capping analogue. Accordingly, photovoltaic devices were fabricated using these control ETLs and benchmarked against the continuously graded ETL device.

Pure PA-capped SnO_2 device: Despite exhibiting nearly identical band alignment and interfacial passivating chemistry at the perovskite/ETL interface to the graded device (**Fig. S11a**), its performance remained notably lower, particularly in open circuit voltage (V_{oc}) (26.60% vs. 27.64%, in **Figs. S11b**, **c**). This disparity directly implicated the graded doping as the origin of the enhanced V_{oc}.

Mixed PA/SA-capped SnO_2 device: Although this ETL possesses similar bulk ligand composition, the device achieved only 26.64% efficiency, which was markedly below the 27.64% of the graded device (**Figs. S11b**, **d**).

Collectively, these comparisons showed that neither interfacial passivation alone (pure PA) nor bulk ligand mixing alone (mixed PA/SA) can reproduce the performance gain; the graded distribution is essential.

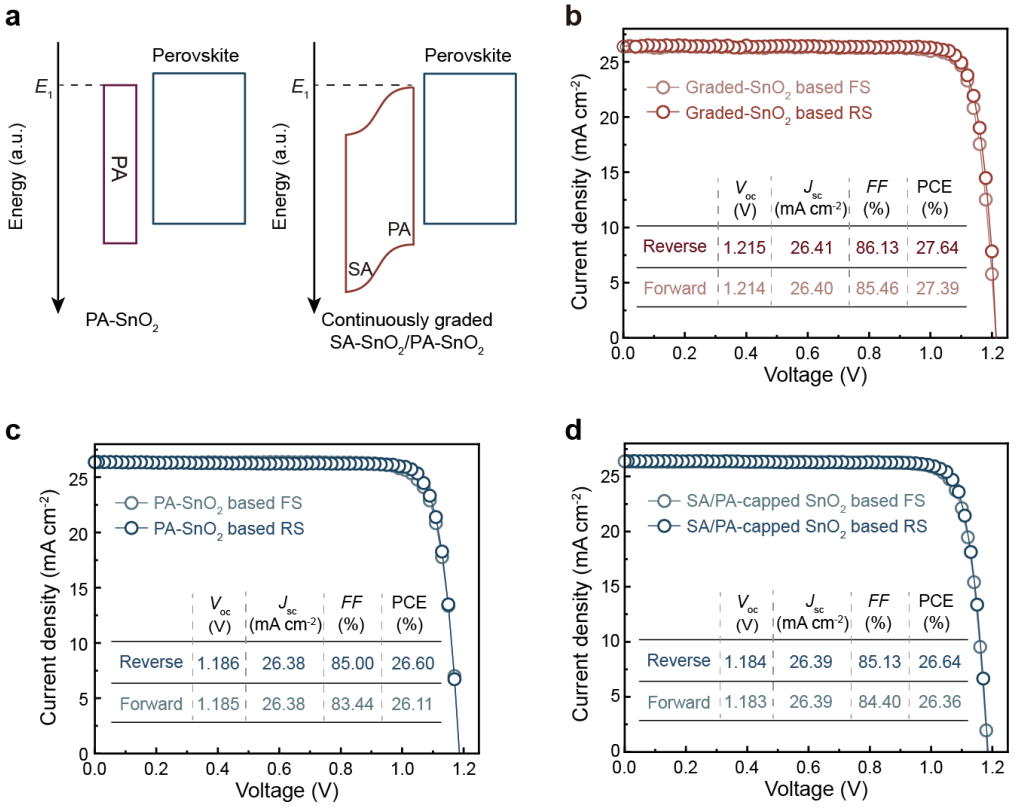

Fig. S11. *(**a**) Schematic diagrams of devices stacks based on PA-SnO_2 and graded-SnO_2. J-V curves of PSCs based on graded-SnO_2 (**b**), PA-SnO_2 (**c**), and mixed-ligand-capped SnO_2 ETL (**d**), respectively.*

2) To understand why the graded structure outperformed homogeneous ligand capping, we combined TRPL measurements with SCAPS-1D simulations.

As shown in **Table 1** (previous response to Comment 1), the graded ETL/perovskite interface exhibited a faster electron-transfer rate (k_{ET} = 4.18 × 10^7 s^{-1}) and higher extraction efficiency (η_{ET} = 99.19%) compared to the bilayer counterpart (which itself represents a discrete, non-continuously graded structure). When comparing the graded ETL to the homogeneous PA-capped ETL (which has identical interface chemistry), TRPL measurements still revealed a faster electron extraction at the graded interface (**Fig. S12a**). To further quantify these differences, the electron-transfer rate (k_{ET}) and extraction efficiency (η_{ET}) for PA-capped interface were also calculated and were summarized in **Table 3**. The results confirmed that the graded interface consistently maintained superior charge transfer characteristics, with higher electron-transfer rate (k_{ET}) and extraction efficiency (η_{ET}) than that of PA-capped ETL (2.5 × 10^7 s^{-1} and 98.72%; **Table 3**). This indicated that the graded doping modifies the internal electric field profile, facilitating more efficient drift of photogenerated electrons toward the ETL and reducing interfacial accumulation, a benefit that pure chemical passivation cannot provide.

To further substantiate this conclusion, we performed SCAPS-1D simulations comparing pure PA-capped SnO_2 and graded SnO_2 under identical interface defect density and band alignment (**Supplementary Table 2**). The graded structure yielded a higher simulated efficiency, attributed to an enhanced built-in electric field that facilitates charge extraction and suppresses recombination (**Fig. S12b**). This simulation outcome aligns quantitatively with the experimental trends, reinforcing that the graded doping, not merely ligand passivation, is responsible for the improved device performance.

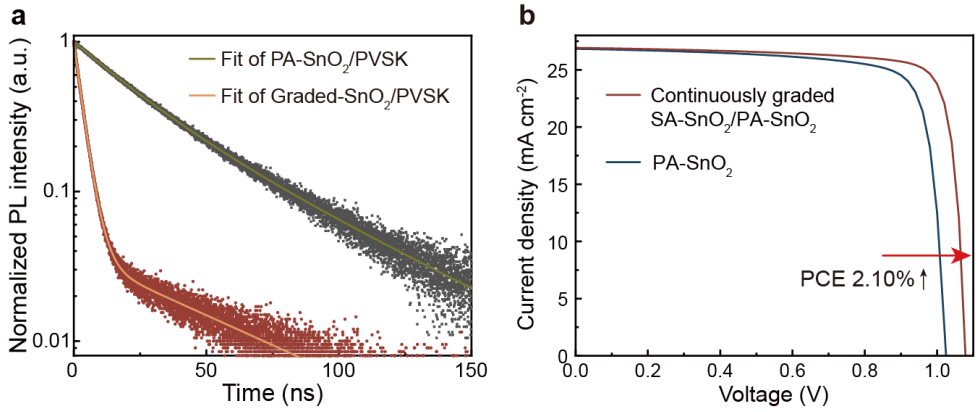

Fig. S12. *(**a**) TRPL spectra of PA-SnO_2/perovskite and continuously graded SnO_2/perovskite stacks. (**b**) Simulated J-V curves based on PA-SnO_2 and continuously graded SnO_2 ETL.*

Table 3. TRPL fitting parameters for PA-SnO_2/perovskite and graded-SnO_2/perovskite stacks.

Sample	τ_{ave} (ns)	k_{ET} (s^{-1})	η (%)
PA-SnO_2/perovskite	39.96	2.5×10^7	98.72
Continuously graded-SnO_2/perovskite	23.9	4.18×10^7	99.19

In summary, these control experiments, TRPL kinetics, together with simulations, provided compelling evidence that the 27.17% certified efficiency stems from the successful construction of a continuously graded doped SnO_2 layer *via* the ligand-competitive binding strategy, rather than from a simple passivation effect of the ligands. The graded architecture optimizes the internal electric field and carrier dynamics in a way that homogeneous ligand capping cannot achieve.

Action: We have now confirmed that the enhanced efficiency originates from the continuously graded SnO_2 structure rather than from ligand passivation, through additional control experiments and device simulations (**Supplementary Fig. 19** and **Supplementary Figs. 42-45**). Specifically, we fabricated a series of control devices with different ligand-capping configurations, both at the interface and within the bulk of the SnO_2 ETL, to intentionally vary the degree of surface passivation while preserving or omitting the graded doping profile. The results demonstrated that the graded structure consistently delivered markedly enhanced efficiency, which we attributed to a strengthened built-in electric field that facilitates charge extraction and suppresses recombination. These findings and corresponding discussions have been incorporated into **Supplementary Note 10** (**Pages 37-40**) and the revised manuscript (**Line 190**, **Page 10**; **Line 322**, **Page 18**).

Comment 4. The LCB strategy involves acidic organic ligands (SA and PA) that remain at the SnO_2 surface. How do these residual ligands influence the initial nucleation and grain growth of the overlying perovskite layer? Specifically, is there any evidence of side reactions between the sulfonic/phosphonic acid groups and the lead ions (Pb^{2+}) that might form an insulating intermediate layer (e.g., $PbSO_4$ or Pb-PA complexes)?

Response: We thank the reviewer for this insightful comment regarding the potential influence of residual acidic ligands on perovskite nucleation and the possible formation of insulating interfacial layers. To address these concerns, we have conducted a series of complementary experiments, including contact-angle measurements, *in-situ* PL monitoring, SEM, cross-

sectional TEM, and XPS with argon gas cluster ion beam (GCIB) depth profiling. The results consistently demonstrated that the ligands do not adversely affect perovskite nucleation or grain growth, and no insulating intermediate layer was formed at the buried interface. Detailed experimental evidence and discussion were provided below.

1) To assess whether the surface ligands perturb the initial nucleation and grain growth of the overlying perovskite, we deposited perovskite films on three types of SnO_2 substrates: TGA-capped SnO_2 (control), continuously graded SA-SnO_2/PA-SnO_2 (target structure), and ligand-free SnO_2 fabricated by atomic layer deposition (ALD-SnO_2).

As shown in **Fig. S13**, the perovskite precursor solution exhibited comparable contact angles on all three substrates, indicating similar nucleation behavior. This was attributed to the comparable surface polarity across substrates: both TGA-SnO_2 and graded-SnO_2 were terminated with -COOH groups, while ALD-SnO_2 becomes hydroxyl-terminated (-OH) upon air exposure (*Adv. Mater.* 2023, **35**, 2202447), affording similar wettability.

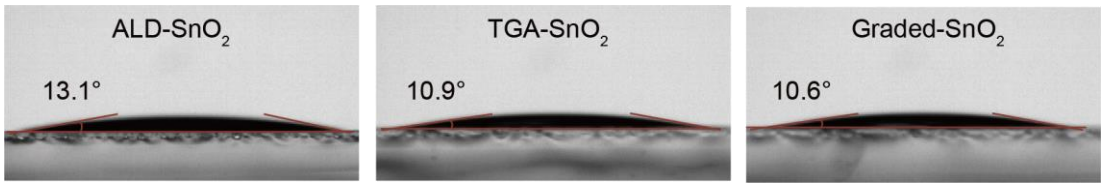

Fig. S13. *Contact angles of perovskite solution upon different SnO_2 substrates.*

We then monitored the perovskite crystallization process during spin coating using *in-situ* time-resolved PL measurements (**Fig. S14**). In all three cases, an intense PL peak centered at ~770 nm, assigned to the perovskite intermediate phase, emerged immediately after antisolvent dripping. The temporal evolution of the peak position followed nearly identical trajectories across substrates, with no observable shift, indicating similar crystallization kinetics and phase-conversion pathways. Furthermore, the full width at half maximum (FWHM) of the PL spectra remained comparable, suggesting that the crystallization quality was unaffected by the underlying substrate.

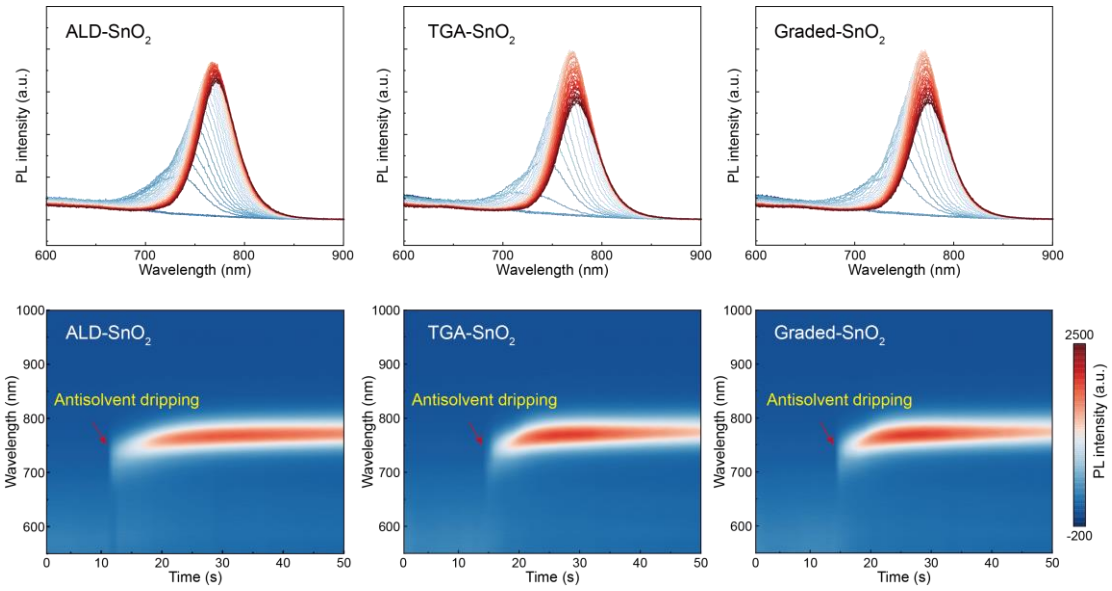

Fig. S14. *In-situ time-resolved PL spectra for perovskite crystallization during deposition on different SnO_2 ETL substrates at spin-coating stage.*

SEM imaging from top-view and buried interfaces (exposed by UV-curable adhesive peeling) revealed that the perovskite films grown on different substrates exhibited nearly identical grain size and morphology (**Fig. S15**).

Collectively, these results confirmed that the residual ligands in the continuously graded SnO_2 do not measurably influence the nucleation, crystallization kinetics, or final grain structure of the overlying perovskite layer.

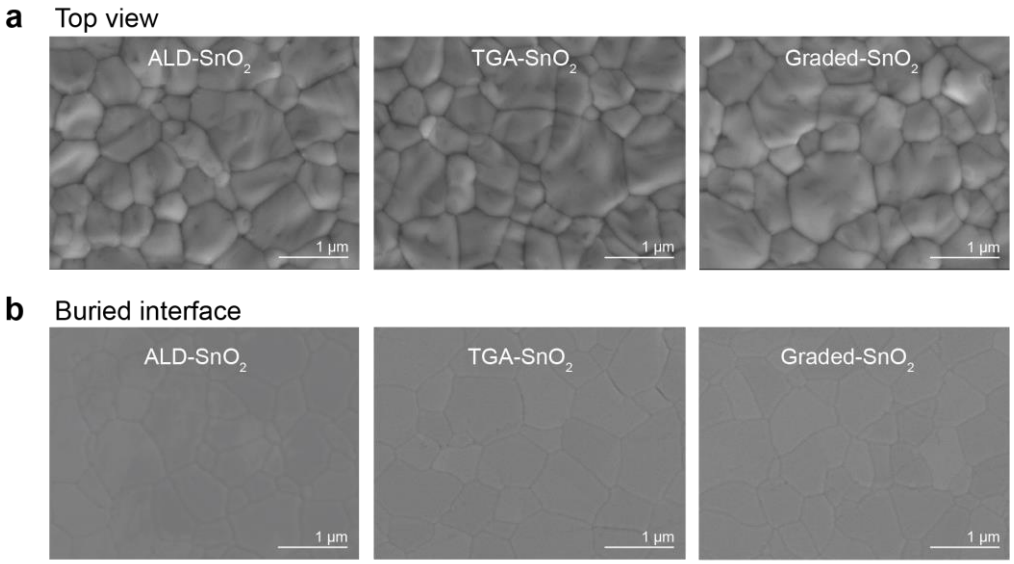

Fig. S15. *SEM images from top view (**a**) and buried interface (**b**) of perovskite layers deposited on different SnO_2 ETL substrates.*

2) To directly investigate whether side reactions between the sulfonic/phosphonic acid groups and Pb^{2+} occur, potentially forming insulating species such as $PbSO_4$ or Pb-PA complexes, we performed cross-sectional TEM and XPS depth profiling.

As shown in **Fig. S16**, a sharp, well-defined interface was observed between the SnO_2 and perovskite layers, with no detectable intermediate layer. This result further confirmed direct contact without amorphous interphase formation.

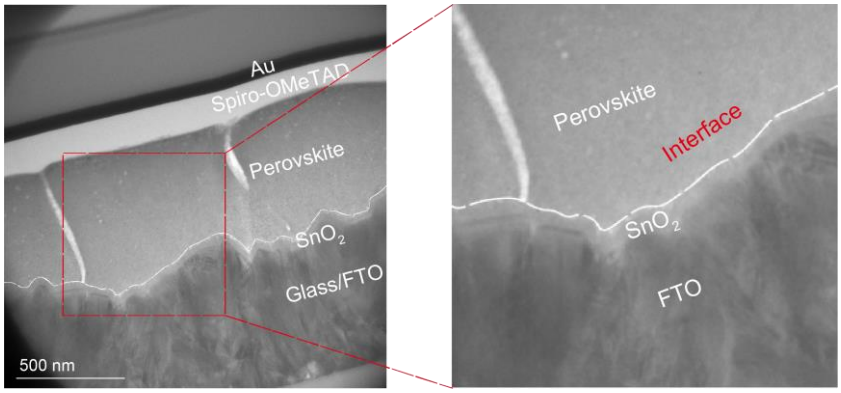

Fig. S16. *TEM images of n-i-p perovskite solar cell.*

To further probe the chemical state at the interface, we conducted XPS measurements with sequential argon cluster ion beam (GCIB) sputtering (**Fig. S17a**). The emergence of the Pb 4*f* signal concurrent with a weak Sn 3*d* signal was used to identify the buried interfacial region. As shown in **Figs. S17b**, **c**, the Pb *4f* spectra acquired from the buried interface exhibited no additional shoulder peaks, no peak shifts, and no broadening compared to those from the bulk perovskite. This indicated that Pb^{2+} remained in its native coordination environment without detectable formation of Pb-sulfonate, Pb-phosphonate, or other insulating lead-based compounds. Consequently, these complementary microscopic and spectroscopic analyses collectively demonstrated that the acidic ligands do not react with Pb^{2+} to form any insulating intermediate species at the buried interface.

In summary, the combined experimental evidence, ranging from wettability, *in-situ* crystallization monitoring, and morphological analysis to interfacial imaging and chemical state profiling, unequivocally showed that the residual ligands in the continuously graded SnO_2 structure do not impede perovskite nucleation or grain growth, nor do they form insulating interfacial layers. The high device performance reported in our manuscript therefore originates from the optimized electronic properties of the graded ETL, rather than from any unintended side reactions at the buried interface.

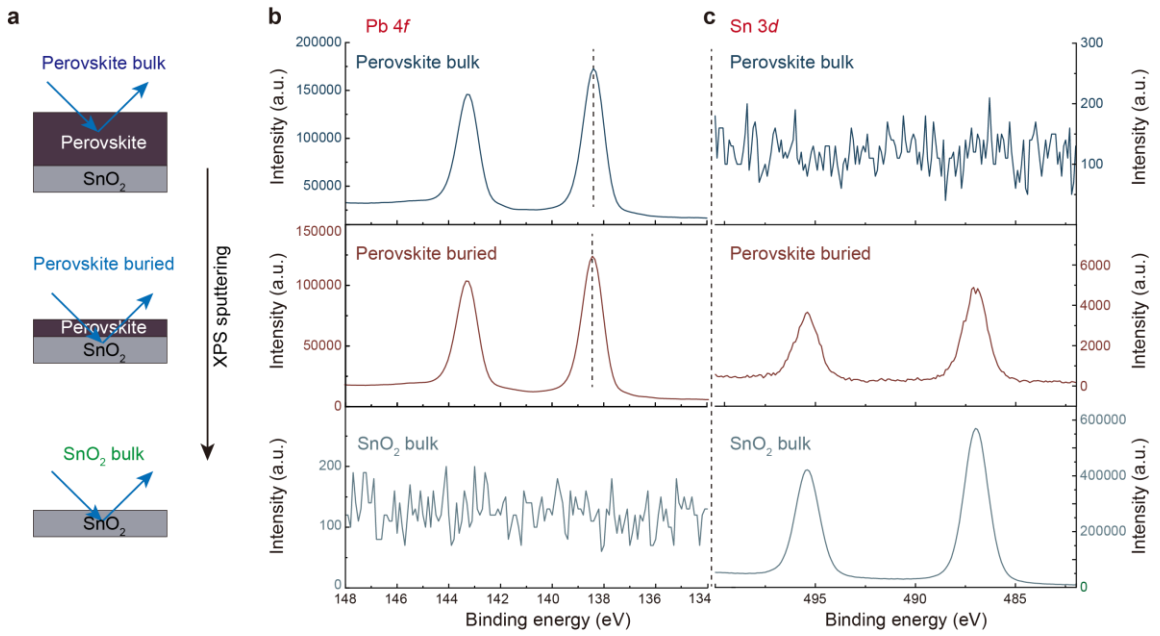

Fig. S17. *(**a**) Schematic illustration of XPS sputtering and signal detection. XPS spectra of Pb 4f (**b**) and Sn 3d (**c**) corresponding to the perovskite bulk, buried interface, and SnO_2 bulk region, respectively.*

Action: We have now confirmed that the ligands do not influence the initial nucleation or grain growth of the overlying perovskite layer, as evidenced by additional contact-angle, *in-situ* PL, and SEM measurements (**Supplementary Figs. 36-38**). Furthermore, we have verified that the ligands do not react with Pb^{2+} to form any insulating intermediate species at the buried interface, based on additional TEM images and sputter XPS analyses (**Supplementary Figs. 39-40**). Detailed analysis and discussion have been incorporated into the revised manuscript (**Line 283, Page 16**) and **Supplementary Note 9**.

Comment 5. The reported J_{sc} of 26.48 mA/cm^2 is exceptionally high. Could the authors clarify the specific mechanisms by which the LCB-SnO_2 strategy contributes to such an enhanced current density?

Response: We thank the reviewer for this insightful comment. To address the origin of the high short-circuit current density (J_{sc}) of 26.48 mA cm^{-2}, we have performed additional high-resolution external quantum efficiency (EQE) measurement to verify its accuracy, and conducted three-dimensional finite-difference time-domain (3D-FDTD) optical simulations to elucidate the underlying mechanisms. Our results showed that the high J_{sc} arose from the synergistic combination of a narrow-bandgap perovskite absorber and enhanced light management enabled by a textured FTO substrate, with a further contribution from improved charge extraction due to the LCB-SnO_2 structure. The detailed evidence was provided below.

1) The bandgap of our perovskite absorber was determined to be 1.51 eV from the UV-vis absorption spectrum and high-resolution EQE measurement (**Fig. S18**). For a semiconductor with this bandgap, the maximum theoretical J_{sc} under AM 1.5G illumination (280 - 4000 nm) is calculated by integrating the solar spectrum from 280 nm to the cutoff wavelength (λ_g = 821 nm), according to the **Equation 4**, under the assumption that all photons with energies above the bandgap are fully absorbed and converted into collected electron-hole pairs. This yields a theoretical upper limit of approximately 28.7 mA cm^{-2}, confirming the experimentally achieved 26.48 mA cm^{-2} is well within the thermodynamic limit.

$$J_{sc} = q\int_0^{\lambda_g} \frac{I(\lambda)\lambda}{hc} d\lambda \qquad 4$$

where, λ_g is the cutoff wavelength corresponding to semiconductor bandgap, $I(\lambda)$ is the AM 1.5G spectral irradiance, q is the elementary charge, h is Planck's constant, and c is the speed of light.

Furthermore, as shown in **Fig. S18b**, the integrated J_{sc} derived from the high-resolution EQE spectrum is 26.20 mA cm^{-2}, which deviates by only ~1% from the measured value, well within typical experimental uncertainty. This close consistency validated the accuracy of the reported current density. Moreover, we have compiled reported J_{sc} values for perovskite solar cells with bandgaps in the range of 1.50 - 1.53 eV (**Table 4**); our value falls squarely within the range of literature reports, further confirming its credibility.

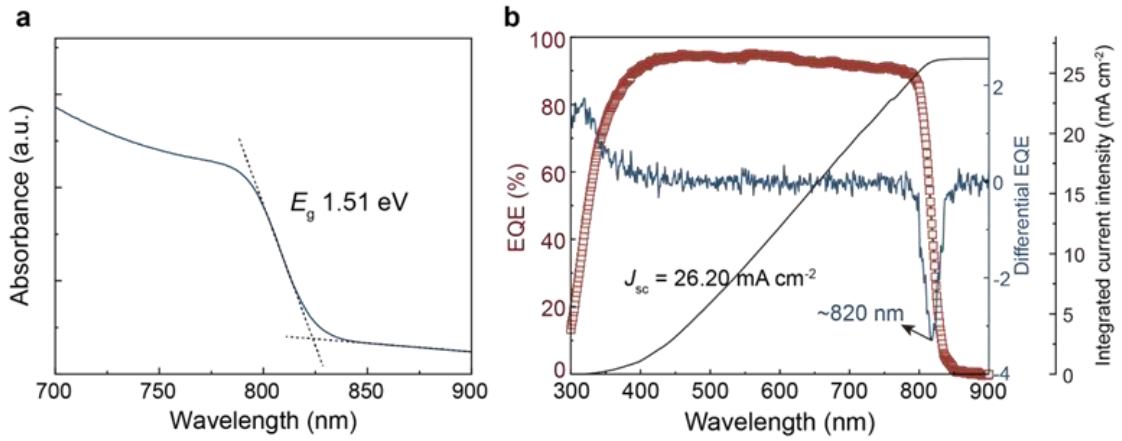

Fig. S18. *UV-vis absorption for perovskite absorber (**a**) and high-resolution EQE spectra (**b**) for LCB-derived SnO_2 based PSCs.*

Table 4. **Summary of the reported device's J_{sc} (certified) based on FTO textured substrate.**

E_g (eV)	Certified J_{sc} (mA cm^{-2})	Steady-state PCE (%)	Ref.
1.51	**26.48**	**27.17**	**This work**
1.53	26.43	26.48 (*JV*)	*Science* 2026, 391, 6781
1.51	26.61	27.18	*Science* 2025, 390, 6773
1.50	26.40	25.8	*Nat. Photon.* 2025, 19, 985
1.53	26.35	25.72	*Nat. Photon.* 2025, 19, 701
1.53	26.43	25.94	*Nature* 2024, 635, 82
1.53	26.38	25.39	Science 2022, 375, 302

2) The high J_{sc} was not attributable to a single factor but rather resulted from a combination of optical and electronic enhancements, which we have deconvoluted through experiments and simulations.

2.1) **Optical contribution: textured FTO substrate.** As described in the manuscript, the FTO substrate used in this work exhibited a pronounced surface texture. Atomic force microscopy (AFM) measurement revealed an RMS roughness of 43.9 nm and pyramid heights up to ~200 nm, compared to conventional FTO substrates (RMS ~12 nm, pyramid height ~60 nm; **Fig. S19**). Such texturing effectively reduces front-surface reflection and increases the optical path length within the perovskite layer, a well-established strategy for enhancing photon harvesting (*Science* 2022, **375**, 302-306; *Nature* 2023, **624**, 289-294).

To quantify the optical contribution, we performed 3D FDTD simulations combined with APSYS software (**Fig. S20**). As the pyramid height increases from 0 to 200 nm, the simulated J_{sc} increases monotonically. Relative to a conventional substrate with 100 nm pyramid height, the 200 nm texture used in our work yields an additional ~0.4 mA cm^{-2} in J_{sc}, unambiguously demonstrating the critical role of substrate texturing in light management.

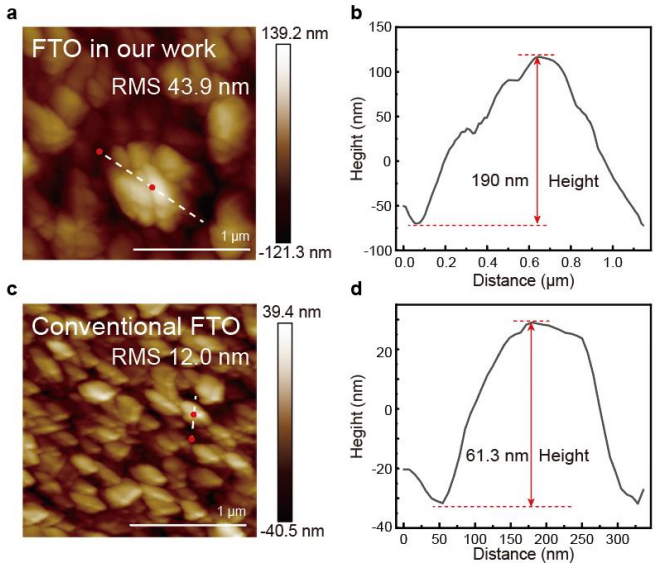

Fig. S19. *AFM images of FTO substrate used in our work (**a**) and a conventional FTO substrate (**c**). Height distribution profiles along the white dashed line region were shown for our FTO substrate (**b**) and the conventional FTO substrate (**d**).*

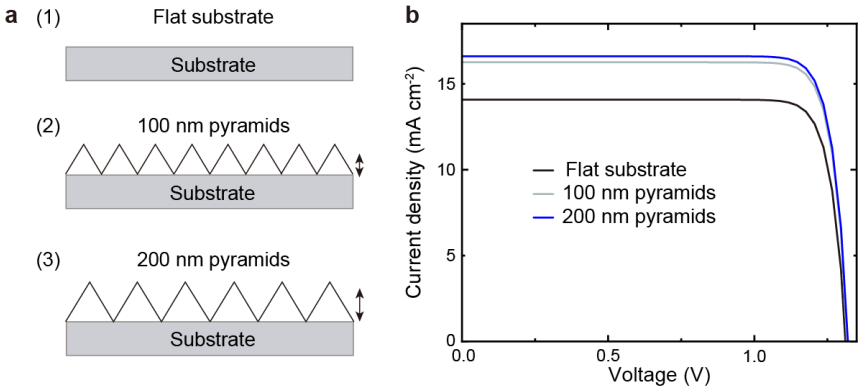

Fig. S20. *(**a**) Schematic illustrations of FTO substrates with pyramids of varying heights. (**b**) Simulated J-V curves of devices based on FTO substrates with different pyramid heights.*

2.2) **Electronic contribution: enhanced charge extraction *via* LCB-SnO_2.** In addition to the optical gain, the CGD-SnO_2 structure itself contributed to the high J_{sc} by improving charge extraction efficiency. As shown in **Fig. 4d** of the manuscript (**Fig. S21**), devices incorporating the continuously graded ETL consistently exhibited higher J_{sc} than control devices, even when fabricated on the same textured FTO. This enhancement originated from the strengthened built-in electric field within the graded ETL, as established by our SCAPS-1D simulations and TRPL measurements (see response to Comment 1). The improved field-driven electron extraction reduces interfacial carrier accumulation and minimizes recombination losses, allowing a larger fraction of photogenerated carriers to be collected as photocurrent.

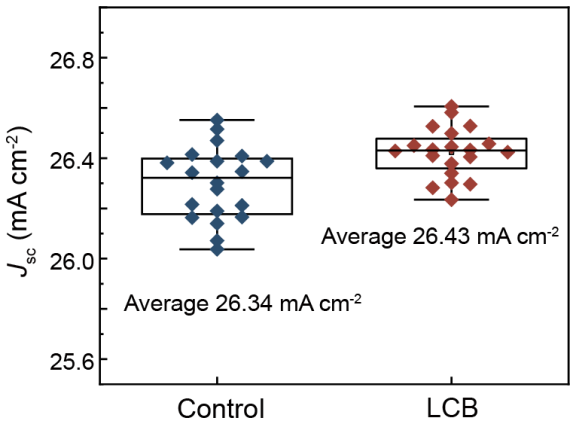

Fig. S21. *Statistical distribution of J_{sc} for 20 devices with control or LCB-derived SnO_2.*

Taken together, our analyses confirmed that the exceptionally high J_{sc} of 26.48 mA cm^{-2} is both accurate and mechanistically well-grounded. It resulted from a narrower bandgap of the perovskite absorber (1.51 eV), which set a high theoretical ceiling; and enhanced light management enabled by a highly textured FTO substrate, contributing approximately 0.4 mA cm^{-2} relative to conventional substrates; as well as, improved charge extraction arising from the CGD SnO_2 ETL, which minimizes recombination losses and maximizes carrier collection. The combination of these optical and electronic enhancements yielded a J_{sc}, while remaining fully consistent with literature values for similarly band-gapped devices.

Action: We have now confirmed the accuracy of the reported J_{sc} of 26.48 mA cm^{-2} through additional high-resolution EQE characterization. We attributed this high current density to the combined effects of a narrow-bandgap absorber and improved light management enabled by the textured FTO substrate, as demonstrated by additional 3D FDTD optical simulations. The corresponding optical simulations and detailed discussions were provided in **Supplementary Note 8** and in the revised manuscript (**Line 263**, **Page 14**; **Line 316**, **Page 18**), and the simulation methodology has been included in the revised Methods section (**Line 493**, **Page 28**).

Comment 6. The certified steady-state efficiency of 27.17% reported in this work is arguably the highest for n-i-p perovskite solar cells and even exceeds the current world record for perovskite cells on the NREL Best Research-Cell Efficiency Chart. Could the authors clarify why this result has not yet been updated on the NREL chart? Furthermore, do the authors have plans to submit this cell for an official NREL or ISFH record listing to verify its standing as a new global benchmark?

Response: We thank the reviewer for this thoughtful comment and for recognizing the significance of our result. Regarding the certified steady-state efficiency of 27.17% reported in this work, we would like to provide the following clarification.

At the time we prepared this manuscript, the "NREL Best Research-Cell Efficiency Chart" and the latest Solar Cell Efficiency Tables (Green, M. et al., Version 66, *Prog. Photovolt. Res. Appl.* **33**: 795-810) already reported a certified single-junction device efficiency of 27.30%, alongside a steady-state PCE of 27.18% published in "*Science* **2025**, 390, 638". Given that these benchmarks were established during the course of our work, our reported steady-state efficiency of 27.17%, while representing the highest value to date for the n-i-p architecture, does not constitute a new overall record for single-junction perovskite solar cells.

We greatly appreciate the reviewer's suggestion regarding official certification. We are actively pursuing further improvements in device performance and will certainly consider submitting future record cells to NREL or ISFH for formal recognition. In the meantime, we have updated the latest reported efficiencies of perovskite solar cells in **Extended Data Fig. 1** and **Supplementary Table 5** to reflect the current state of the field.

Action: We have now updated the latest reported efficiencies of PSCs in **Extended Data Fig. 1** and **Supplementary Table 5**.

Referee #2:

SnO_2 serves as an electron-transport layer in conventional (n-i-p) perovskite solar cells, where its interfacial properties directly govern device efficiency and long-term stability. Despite its importance, optimizing SnO_2 remains a major challenge due to the intricate surface chemistry of its nanocrystals, which often introduces trap states and energy-level misalignment that compromise performance. The graded SnO_2 architecture reported by Yuan et al. offers an effective means to this bottleneck by enabling systematic modulation of surface defects and energy landscapes. This strategic approach delivers substantial gains in power-conversion efficiency while enhancing operational stability, representing a significant advance in the field. The work is suitable for publication in *Nature* after the authors address the following concerns.

Response: We really appreciate the reviewer's endorsement of our work. By carrying out additional experiments and theoretical studies, we have now fully addressed the concerns raised by the reviewer which significantly improved the quality of the manuscript.

Comment 1. As a typical HTL, Spiro-OMeTAD generally shows an electron mobility of less than 10^{-4} cm^2 V^{-1} S^{-1}, usually on the order of 10^{-7} to 10^{-5} cm^2 V^{-1} S^{-1}. This is inconsistent with the measured value of 2.8×10^{-3} cm^2 V^{-1} S^{-1} shown in Supplementary Fig. 6. In addition, is it appropriate to compare the electron mobility of TGA-SnO_2 and Spiro-OMeTAD to state that there is an imbalance in the electron-hole extraction for TGA-SnO_2-based device, given that the main function of Spiro-OMeTAD is to block the electrons rather than transport them?

Response: We thank the reviewer for raising this important point, which allows us to clarify the reported mobility values and the rationale behind our comparison of carrier transport properties.

1) First, we have confirmed that the value of 2.8×10^{-3} cm^2 V^{-1} s^{-1} presented in **Supplementary Fig. 6** corresponds to the **hole mobility** of Spiro-OMeTAD, not its electron mobility. This measurement was performed using the space-charge-limited current (SCLC) method, as detailed in **Supplementary Note 2**, **Page 8**. To avoid any ambiguity, we have now explicitly labeled this quantity as "hole mobility" in the revised **Supplementary Fig. 7** (**Fig. S22**). Furthermore, we have compiled a summary of reported hole mobilities for Spiro-OMeTAD doped with LiTFSI and *t*-BP (**Table 5**), which confirmed that our measured value falls well within the range typically reported in the literature.

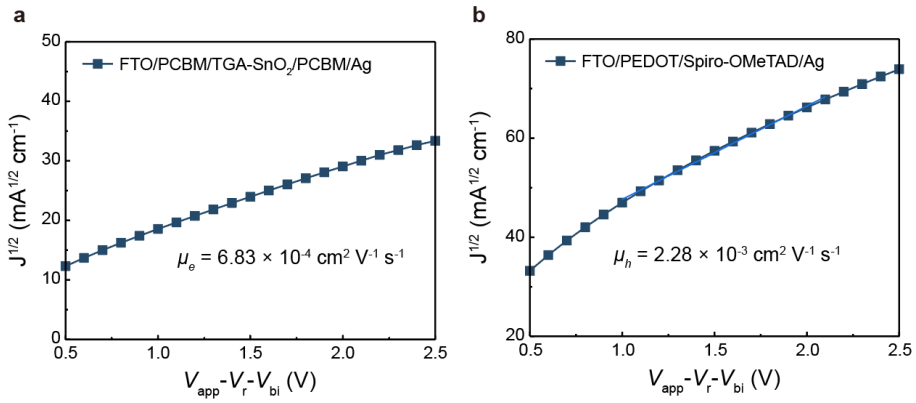

Fig. S22. *SCLC measurements for calculating the electron mobility calculation of TGA-SnO_2 ETL (**a**) and hole mobility calculation of Spiro-OMeTAD HTL (**b**), respectively.*

Table 5. Summary of the reported Spiro-OMeTAD's hole mobility by SCLC measurements.

Spiro-OMeTAD	Hole mobility (cm^2 V^{-1} s^{-1})	Ref.
LiTSFI and *t*BP doped	**2.8×10^{-3}**	**This work**
LiTFSI and *t*BP doped	$10^{-4} \sim 10^{-3}$	*Adv. Mater.* 2025, 37, e13270
LiTFSI and tBP doped	5.11×10^{-3}	*J. Am. Chem. Soc.* 2024, 146, 45, 30893
LiTSFI-doped	$5.0 \times 10^{-3} \sim 1.5 \times 10^{-2}$	*Adv. Mater. Interfaces* 2016, 3, 1600117
LiTSFI-doped	2.65×10^{-3}	*Adv. Energy Mater.* 2024, 2403737
LiTFSI and *t*BP doped	$4.56 \times 10^{-3} \sim 3.2 \times 10^{-3}$	*Adv. Optical Mater.* 2022, 10, 2200802

2) Second, we fully agreed with the reviewer that Spiro-OMeTAD functions primarily as a hole-transport layer (HTL) and serves to block electrons. In our original manuscript, the comparison was not intended to evaluate electron transport in Spiro-OMeTAD, **but rather to assess the balance between electron extraction in the electron-transport layer (ETL) and hole extraction in the HTL**. Given that electrons and holes are generated in equal numbers upon photoexcitation, efficient device operation requires that both extraction pathways be comparably rapid. Our data showed that the electron mobility of the TGA-SnO_2 ETL is substantially lower than the hole mobility of Spiro-OMeTAD, leading to an imbalance where holes are extracted more efficiently than electrons. This imbalance results in carrier accumulation at the ETL/perovskite interface and increased nonradiative recombination, an effect that is mitigated by the continuously graded SnO_2 structure. To clarify this point, we have revised the corresponding statement in the supporting information (**Supplementary**

Note 2, **Page 7**) to explicitly indicate that the comparison reflects the relative rates of electron and hole extraction across the two transport layers, rather than a direct comparison of electron transport between SnO_2 and Spiro-OMeTAD.

In summary, we have now clarified that the reported mobility value corresponds to hole transport in Spiro-OMeTAD, and we have refined the interpretation of the carrier transport balance to accurately reflect the distinct roles of the ETL and HTL. These revisions are incorporated in the updated supplementary information and are consistent with the main text. We appreciate the reviewer's careful reading and constructive feedback.

Action: We have now confirmed that the value of 2.8×10^{-3} cm^2 V^{-1} s^{-1} corresponds to the hole mobility of Spiro-OMeTAD, and **Supplementary Fig. 7** has been updated accordingly. Accordingly, we have now clarified that the electron-hole extraction imbalance observed in TGA-SnO_2 based devices arises from the sluggish electron mobility of SnO_2 relative to the hole mobility of Spiro-OMeTAD. The corresponding statement has been revised in the supporting information (**Supplementary Note 2**, **Page 7**) and in the revised manuscript (**Line 98**, **Page 5**).

Comment 2. The oxygen vacancies (V_o) concentration plays an important role in the properties of SnO_2 layer. The authors have conducted a specific analysis of the minimum electrostatic potential (φ_{min}) and the Sn^{2+}/Sn^{4+} ratio for different ligands, including TGA, MA, PA and SA (Fig. 1d and 1g). However, it appears that there is no clear relationship between φ_{min}, the Sn^{2+}/Sn^{4+} ratio and V_o in the manuscript. The authors should clarify and comment on this point.

Response: We thank the reviewer for this insightful comment, which prompted us to more systematically elucidate the relationship between the molecular properties of the ligands, the resulting Sn^{2+}/Sn^{4+} ratio, and the concentration of oxygen vacancies (V_o) in the SnO_2 films. Through additional cyclic voltammetry (CV) and ^{119}Sn-NMR measurements, we have now established a clear mechanistic link between these parameters. Details of the experiments and discussion were provided below.

As shown in **Figs. S23 a**, **b**, the minimum electrostatic potential (φ_{min}) of the ligand head group followed the order MA < PA < SA. A lower φ_{min} corresponds to a more electron-rich functional group, indicating stronger electron-donating ability. Conversely, SA possesses the highest φ_{min}, which exhibits the strongest electron-withdrawing character among the three bidentate ligands, thereby donating the fewest electrons to the adjacent Sn^{2+} ions upon coordination.

This trend in electron donation is directly reflected in the newly added ^{119}Sn-NMR (**Fig. S23d**). As the electron-withdrawing strength of the ligand increases, the ^{119}Sn resonance peaks shift progressively toward higher chemical shift values, indicating a continuous decrease in electron density surrounding the Sn^{2+} centers. This spectroscopic evidence confirmed that the ligand's electronic properties are effectively transduced to the Sn^{2+} ions.

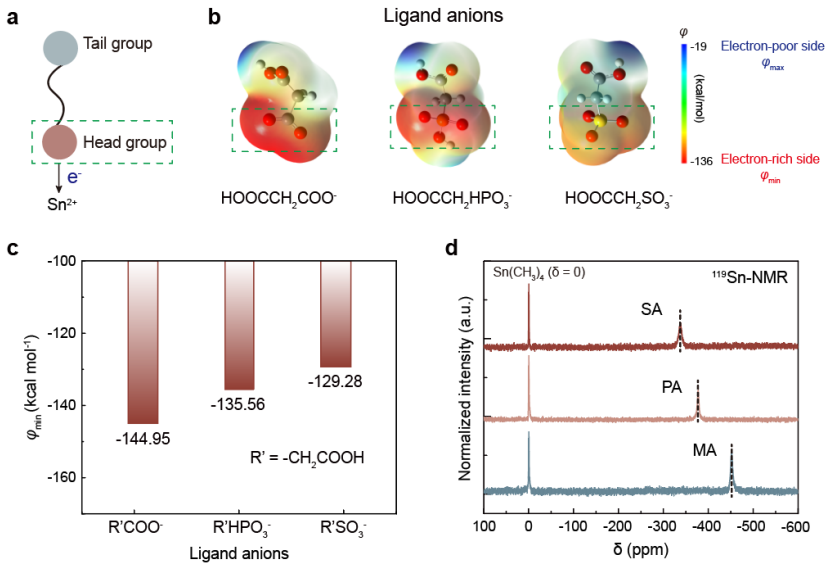

Fig. S23. *(**a**) Schematic illustration of the interaction between bidentate ligands and Sn^{2+}. (**b**) Molecular structures and electrostatic potentials of different ligand anions. (**c**) φ_{min} of each bidentate ligand head-group anion. (**d**) ^{119}Sn-NMR spectra with different ligand treatments.*

The reduced electron density around Sn^{2+} in turn altered its redox behavior. Cyclic voltammetry measurements (**Fig. S24a**) showed that ligands with stronger electron-withdrawing ability induce a more positive Sn^{2+}/Sn^{4+} oxidation potential, meaning that Sn^{2+} becomes more difficult to oxidize. Consequently, a higher fraction of Sn^{2+} remains in the as-deposited SnO_2 film, as corroborated by XPS analysis.

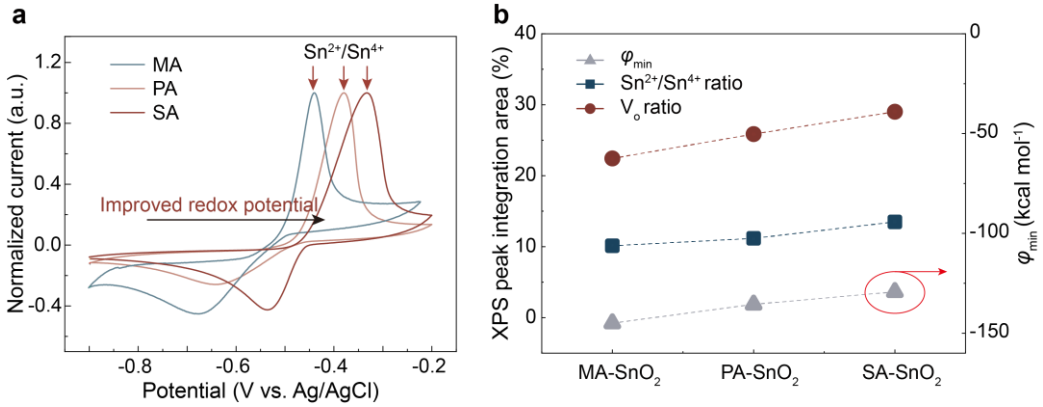

Fig. S24. *(**a**) Sn^{2+}/Sn^{4+} redox potential under different ligands deposition measured by CV. (**b**) The relationship between φ_{min} of bidentate ligands, Sn^{2+}/Sn^{4+}, and V_o area ratios extracted from XPS spectra of SnO_2 ETLs capped with different ligands.*

To maintain lattice charge neutrality, a well-established principle in SnO_2 chemistry (*Nature* **2021**, 590, 587-593), the incomplete oxidation of Sn^{2+} promotes the formation of oxygen vacancies within the SnO_2 lattice. Thus, a higher Sn^{2+}/ Sn^{4+} ratio correlates directly with a higher concentration of oxygen vacancies.

In summary, the complete mechanistic relationship is summarized in **Fig. S24b**: a higher φ_{min} of the bidentate ligand head group leads to stronger electron withdrawal from Sn^{2+}, which suppresses Sn^{2+} oxidation, resulting in a higher Sn^{2+}/ Sn^{4+} ratio and, consequently, a higher concentration of oxygen vacancies in the SnO_2 film. This chain of causality, spanning from molecular electrostatic potential to macroscopic defect chemistry, provides a coherent framework for understanding how ligand design influences the electronic properties of SnO_2 in our graded ETL architecture.

Action: We have now clarified the relationship among φ_{min}, the Sn^{2+}/Sn^{4+} ratio, and oxygen vacancies in the revised manuscript (**Line 150**, **Page 8** and **Line 158**, **Page 9**) and **Supplementary Note 4** (**Pages 12-14**). Specifically, a higher φ_{min} of the bidentate ligand head group leads to an increased Sn^{2+}/Sn^{4+} ratio and consequently a higher concentration of oxygen vacancies in the SnO_2 film. Accordingly, we have added the ^{119}Sn-NMR measurements and a schematic summarizing this relationship in **Supplementary Fig. 13** and **Supplementary Fig. 14**, respectively.

Comment 3. According to the trend in the minimum electrostatic potential (φ_{min}) of φ_{min} MA < φ_{min} PA < φ_{min} SA (Line 144, Page 7; Fig. 1d and Supplementary Fig. 11), the authors predict that the SA-capped SnO_2 NPs would yield the highest V_o concentration and the best band alignment at the buried interface. Does there exist any bidentate ligand with a higher φ_{min}? Or can such ligands be synthesized?

Response: We appreciate the reviewer for this thoughtful and forward-looking question. Based on our established correlation between the minimum electrostatic potential (φ_{min}) of bidentate ligands and the resulting defect chemistry of SnO_2, we have now explored whether ligands with φ_{min} values higher than that of SA exist, and if so, whether they could offer further advantages for device performance. Details of the experiments and discussion were provided below.

1) As outlined in our manuscript (**Line 145**, **Page 8**; and **Supplementary Note 3**), bidentate ligands suitable for chemical bath deposition of SnO_2 must meet several criteria: (i) solubility in acidic aqueous solutions, (ii) oxygen-containing acid head groups with low pK_a values, and (iii) short-chain or phenyl-based backbones to ensure monomeric nanoparticle growth and adequate film conductivity.

Using these screening criteria, we performed DFT calculations on 12 different candidate ligands, systematically varying the head group chemistry and introducing electron withdrawing substituents on the aromatic backbone. As shown in **Fig. S25**, the calculated φ_{min} values range from -142.62 to -119.52 kcal/mol. Notably, several molecules, including compounds (4) through (12), exhibited φ_{min} values higher than that of SA (-129.28 kcal/mol), confirming that bidentate ligands with stronger electron-withdrawing character than SA are indeed accessible, either commercially or synthetically.

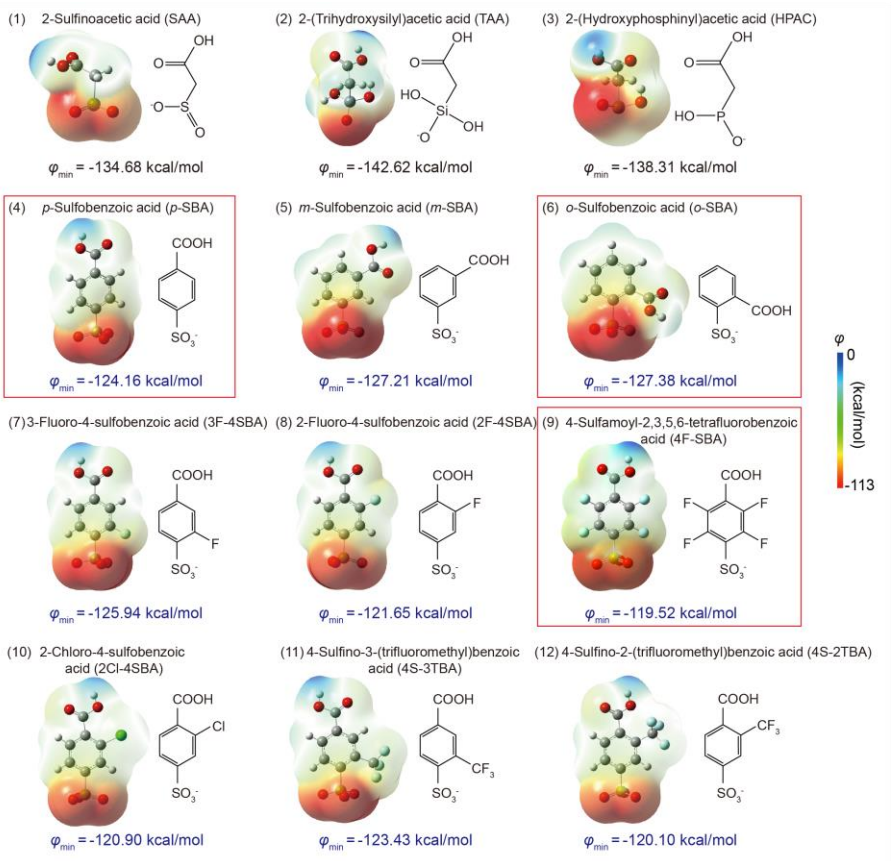

Fig. S25. *Molecular structures and electrostatic potentials of different bidentate ligand anions.*

2) To experimentally evaluate the impact of such higher φ_{min} ligands on resulting SnO_2 properties, we herein selected three commercially available candidate ligands: *o*-SBA (-127.38 kcal/mol), *p*-SBA (-124.16 kcal/mol), and 4F-SBA (-119.52 kcal/mol), all of which possess φ_{min} values higher than SA (highlighted in the red box in **Fig. S25**). Consistent with the trend established in our manuscript, SnO_2 films deposited using these ligands exhibited a progressive upward shift in both the Fermi level and the conduction band minimum (CBM) with increasing φ_{min} (**Figs. S26** and **S27**). These results validated that the ligand's electrostatic potential serves as a reliable descriptor for modulating the electronic structure of SnO_2.

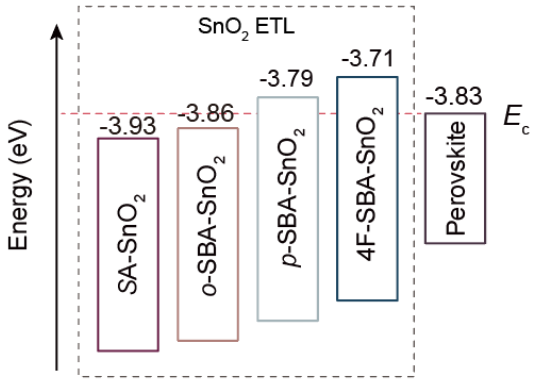

Fig. S26. *Band structure diagrams derived from UPS spectra for SA, o-SBA, p-SBA, and 4F-SBA-SnO₂-capped SnO₂.*

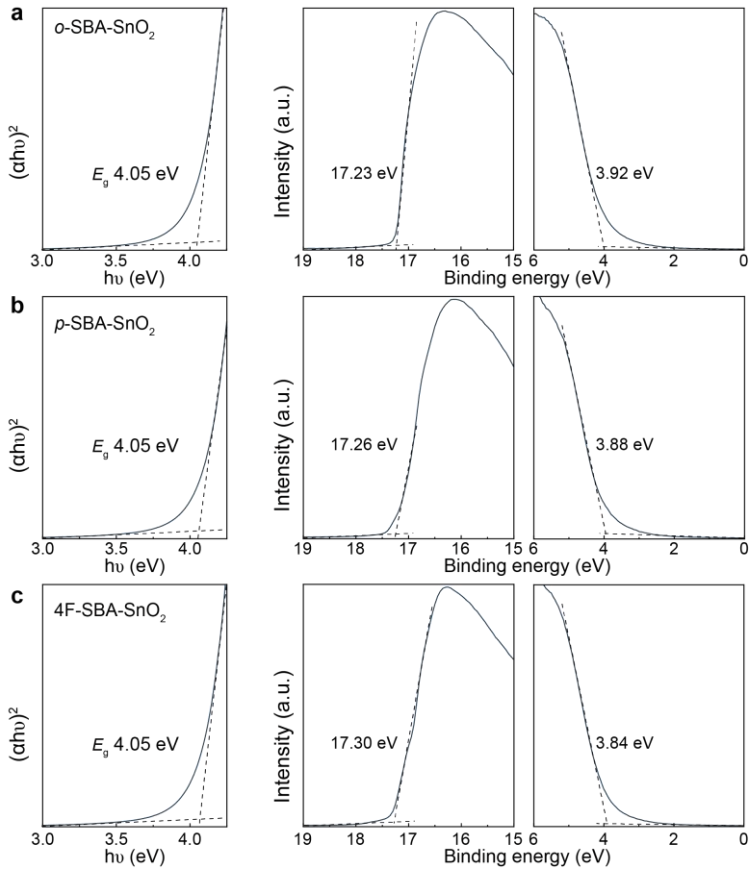

Fig. S27. *UV-vis absorption (left) and secondary electron cut-off region and valence photoemission spectra (right) of UPS spectra for o-SBA-SnO₂ (**a**), p-SBA-SnO₂ (**b**), 4F-SBA-SnO₂ (**c**), respectively.*

3) Given that higher φ_{min} leads to a higher oxygen vacancy concentration and an upward-shifted CBM, we anticipated that such ligands might further optimize the SnO_2/perovskite interface. However, when these SnO_2 ETLs were integrated into devices using the same perovskite absorber, no improvement in efficiency was observed; in some cases, performance deteriorated relative to the SA-based control (**Fig. S28**).

This outcome was attributed to the critical role of band alignment. While a higher φ_{min} increases the SnO_2 CBM, excessively large CBM offsets can introduce an undesirable energetic barrier at the electron extraction interface, impeding charge transfer and increasing recombination. In other words, φ_{min} is not a parameter to be maximized in isolation; rather, its optimal value depends on the specific perovskite composition and the desired alignment of energy levels.

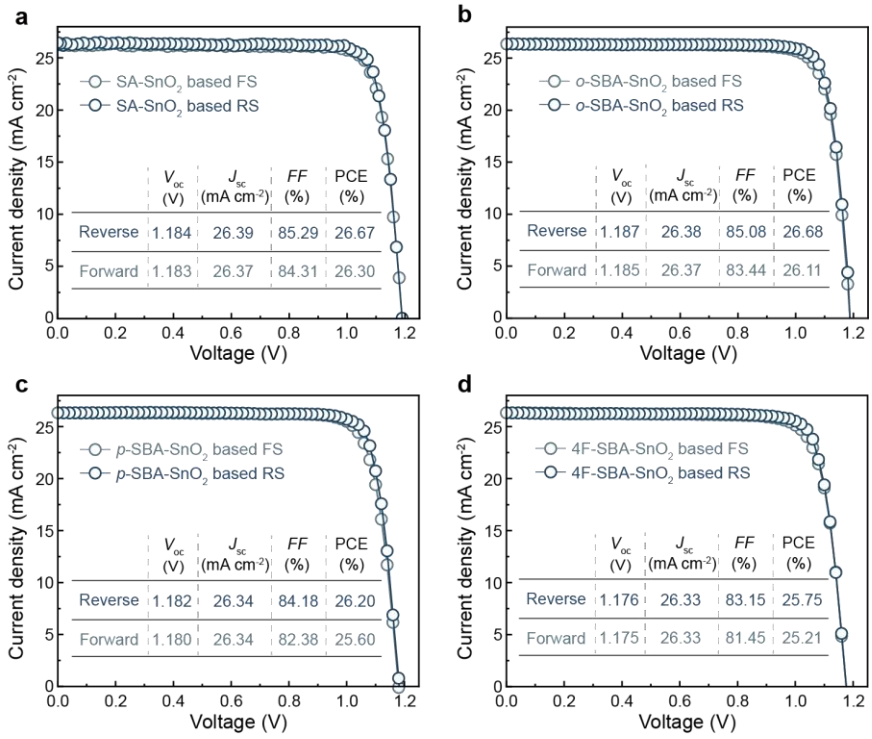

Fig. S28. *J-V curves for SA-SnO_2* ***(a)****, o-SBA-SnO_2* ***(b)****, p-SBA-SnO_2* ***(c)*** *and 4F-SBA-SnO_2* ***(d)*** *based devices, respectively.*

In summary, we have now confirmed that bidentate ligands with φ_{min} values exceeding that of SA do exist and are synthetically or commercially accessible. These ligands modulated the electronic properties of SnO_2 in a predictable manner, consistent with the mechanistic framework established in our work. However, for high-performance device fabrication, the optimal φ_{min} must be carefully matched to the perovskite absorber to minimize band misalignment and avoid interfacial barriers. This insight reinforces the broader principle that the LCB strategy offers a tunable platform, not simply a single optimal ligand, allowing interface engineering to be tailored for different perovskite compositions.

Action: We have now confirmed that bidentate ligands with φ_{min} values higher than that of SA do exist and can be successfully applied in CBD SnO_2 deposition. These ligands modulated the electronic properties of the resulting SnO_2 in a predictable manner, consistent with the mechanistic framework established in our work. However, the optimal φ_{min} must be carefully matched to the perovskite absorber to minimize band misalignment and avoid interfacial

barriers. The corresponding DFT calculations of electrostatic potential were provided in **Supplementary Fig. 17**, and the detailed discussion was included in **Supplementary Note 4** (**Pages 16-18**) and in the revised manuscript (**Line 178**, **Page 10**).

Comment 4. What is *quasi*-layer by layer (*quasi*-LBL)?

Response: We thank the reviewer for this clarifying question. The term "*quasi*-layer-by-layer (*quasi*-LBL)" in our work is introduced to describe a nanoparticle-mediated sequential electrostatic assembly process that parallels classical layer-by-layer film growth, yet with a distinct structural feature. The detailed experiments and discussion are provided below.

As detailed in **Supplementary Note 3**, the SnO_2 ETL fabricated *via* chemical bath deposition relies on ligand-assisted electrostatic adsorption between colloidal SnO_2 nanoparticles and the FTO substrate. Cross-sectional TEM imaging (**Fig. S29**) revealed that the resulting film consists of uniformly stacked 3-5 nm nanoparticles, rather than forming a continuous, homogeneous layer. This particulate assembly is the basis for the prefix "*quasi*", it retains the layer-by-layer growth motif but with discrete nanoparticles as the fundamental building units.

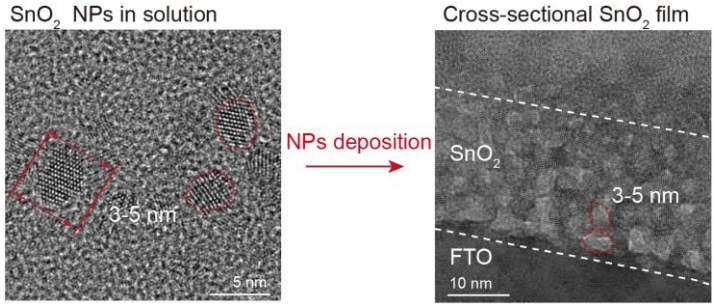

Fig. S29. *TEM image of SnO_2 NPs (3-5 nm) dispersed in solution (left), and cross-sectional TEM image of final SnO_2 film (right).*

Furthermore, the evolution of film thickness with deposition time (**Fig. S30**) exhibited a monotonic increase, confirming that the film grows through successive stacking of nanoparticle layers. In contrast to conventional LBL processes that deposit molecular or ionic layers, our method proceeds *via* sequential adsorption of nanoparticle monolayers, giving rise to a film that is both layer-assembled and nanostructured. We thus refer to this growth mode as "*quasi*-layer-by-layer" to accurately capture its hybrid nature, which combines the ordered stacking characteristic of LBL with the discrete nanoparticle architecture inherent to colloidal assembly.

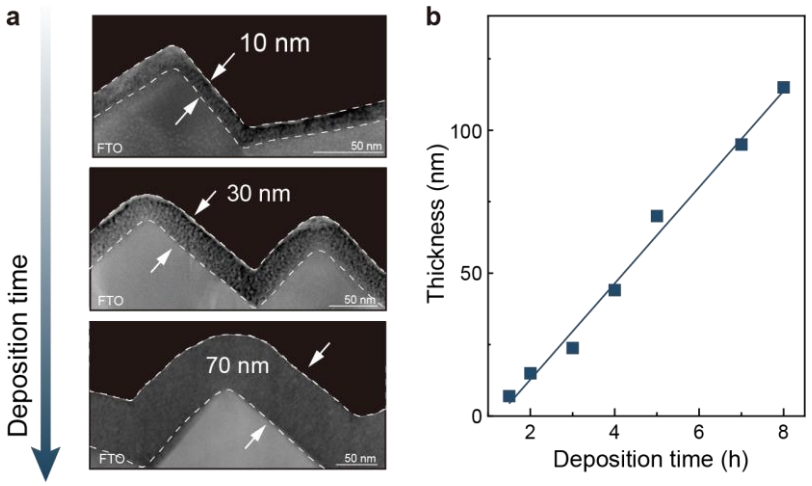

Fig. S30. *(**a**) Cross-sectional HAADF-STEM images of SnO_2 ETLs under varying deposition time. (**b**) SnO_2 films thickness versus deposition time profile.*

In summary, the CBD SnO_2 film evolves through nanoparticle-based sequential assembly, distinct from continuous layer deposition, and was therefore accurately described as a "*quasi*-layer-by-layer" process. This terminology captures both the ordered stacking characteristic of classical LBL and the discrete nanoparticle architecture inherent to our colloidal assembly approach.

Action: We have now clarified the definition of the "*quasi*-layer-by-layer" concept in the revised manuscript (**Line 116**, **Page 6**), with a more detailed discussion provided in **Supplementary Note 3** (**Page 9**).

Comment 5. How do the authors precisely control and monitor the hydrolysis of DMPA? This may be a key factor for the reproducibility of the manuscript.

Response: We really appreciate the reviewer for this important question regarding the control and monitoring of DMPA hydrolysis, which is indeed critical for the reproducibility of our graded SnO_2 deposition. To address this, we have established a quantitative framework combining real-time ^{31}P-NMR tracking with first-order kinetic modeling, enabling precise prediction and control of the hydrolysis process. The detailed experiments and discussion were provided below.

1) Real-time monitoring of DMPA hydrolysis: The hydrolysis kinetics of DMPA were monitored directly during the chemical bath deposition process using ^{31}P-NMR spectroscopy, which provides well-resolved spectral signatures for DMPA and its hydrolysis product, phosphonic acid (PA), with H_3PO_4 as an internal standard (**Fig. S31a**). Spectra were acquired at 0.5 h or 1 h intervals throughout the deposition. By integrating the peak areas corresponding

to PA and DMPA, we quantified the PA conversion rate (x) as a function of time, which increased from 2.6% at 1 h to 9.4% at 5 h (**Fig. S31b**).

Fitting the conversion data to a first-order kinetic model yielded the rate equation: "$[A] = [A]_0 \exp(-4.845 \times 10^{-6}\, t)$" and "$\ln(1-x) = -4.845 \times 10^{-6}\, t$", describing the conversion from DMPA to PA (**Fig. S32**) ($[A]_0$ and $[A]$ denote the initial and time-dependent concentrations of DMPA, respectively). This model quantitatively described the conversion from DMPA to PA under our deposition conditions.

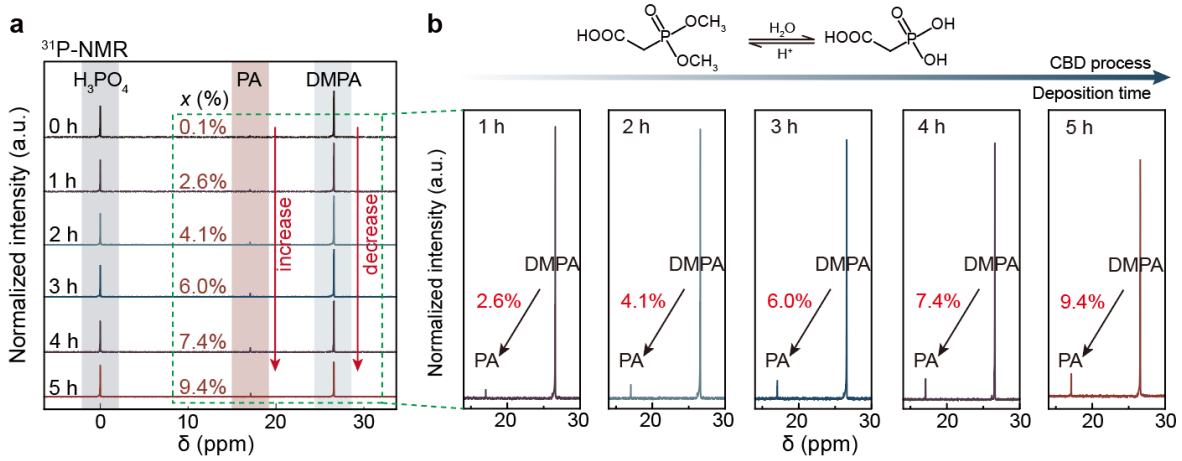

Fig. S31. *(**a**) ^{31}P-NMR spectra of DMPA into PA at different deposition times during CBD process, with H_3PO_4 used as the internal standard. (**b**) Enlarged ^{31}P-NMR spectra of DMPA to PA during CBD process.*

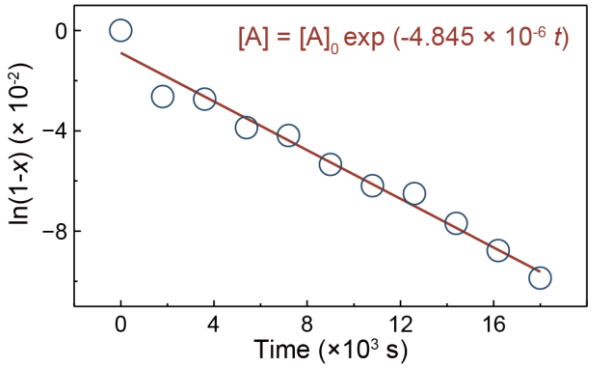

Fig. S32. *Extracted PA conversion rate (x) from ^{31}P-NMR data and the corresponding first-order hydrolysis kinetic fit.*

2) Control for reproducible film formation: Based on the kinetic model, the concentrations of residual DMPA and liberated PA at any deposition time can be accurately predicted. This predictive capability allows us to rationally design the initial precursor composition to achieve a target PA concentration at a desired deposition time. For example, to obtain a PA concentration of ~0.15 mM after 4 h of deposition, the required initial DMPA concentration is

calculated to be 2.1 mM. Such precision ensures that the graded SnO_2 structure, which relies on a controlled gradient in ligand composition, can be reproducibly fabricated across batches.

In summary, we have established a robust methodology for monitoring and controlling DMPA hydrolysis through real-time ^{31}P-NMR analysis and first-order kinetic modeling. This framework enabled precise adjustment of the initial precursor conditions to achieve reproducible formation of the continuously graded SnO_2 ETL, thereby addressing the reproducibility concern raised by the reviewer. The detailed procedures and kinetic analysis are now included in the revised supporting information.

Action: We have now provided a detailed analysis of the precise control of DMPA hydrolysis in **Supplementary Note 6** (**Page 22**). Specifically, the hydrolysis process was quantitatively monitored through real-time ^{31}P-NMR tracking and fitted to a first-order kinetic equation. Accordingly, we have updated **Fig. 2e** and **Fig. 2f**. The corresponding discussion has been incorporated into the revised manuscript (**Line 237**, **Page 13**).

Comment 6. In general, for the $SnCl_2$-based CBD process, the solution is typically acidic, with a pH value of around 1-2. The authors also mention in Supplementary Note 3 that a strongly acidic environment induces deprotonation of carboxyl groups, driving electrostatic adsorption onto the FTO substrate. However, in Fig. 2a, the chemical equation show that the reverse reaction of DMPA hydrolysis may occur under H^+-rich conditions, suggesting that DMPA is more likely to remain stable in an acidic environment. Therefore, is it possible that DMPA does not fully undergo hydrolysis under these conditions? If so, the final ETL structure may be a SA-SnO_2/ DMPA-SnO_2 gradient, rather than the proposed SA-SnO_2 (n^+)/ PA-SnO_2 (n) gradient. The authors should provide compositional identification of the ETL intermediate prior to annealing at 170 °C to clarify this issue.

Response: We thank the reviewer for this insightful question. We have now confirmed by ^{31}P-NMR that DMPA undergoes controlled partial hydrolysis in the acidic CBD solution, serving as a slow-release precursor for PA ligands rather than being fully hydrolyzed. We have also performed additional experiments and theoretical analyses to clarify the chemical composition of the ETL prior to annealing, confirming that the as-deposited (prior to annealing at 170 °C) structure was indeed the intended SA-SnO_2 (n^+)/PA-SnO_2 (n) graded, rather than an SA-SnO_2/ DMPA-SnO_2 graded. The detailed experiments and discussion were provided below.

1) We have now clarified that DMPA undergoes partial hydrolysis under acidic conditions, as designed. Real-time ^{31}P-NMR (**Fig. S31**) showed that during the acidic CBD process, the integrated peak area of DMPA gradually decreased while that of PA increased with deposition

time. This confirmed that DMPA undergoes progressive hydrolysis to release PA, but the conversion was not complete, reaching only ~9.4% after 5 h. This partial hydrolysis is not a limitation but rather a deliberate feature of our strategy: DMPA serves as a "slow-release precursor" that continuously supplies PA ligands over the deposition period, enabling the formation of a graded ligand distribution without requiring full conversion.

2) To directly assess whether DMPA itself incorporates into the film, we fabricated SnO_2 ETLs using DMPA as the sole additive and performed TOF-SIMS analysis on the as-deposited film prior to annealing (**Fig. S33**). Across the entire film depth, no ester-related fragments characteristic of DMPA were detected. Instead, PO_2^- signals, originating from the hydrolyzed PA ligand, were uniformly distributed throughout the SnO_2 layer. These results unequivocally demonstrated that the deposited film consists of PA-capped SnO_2, not DMPA-capped SnO_2.

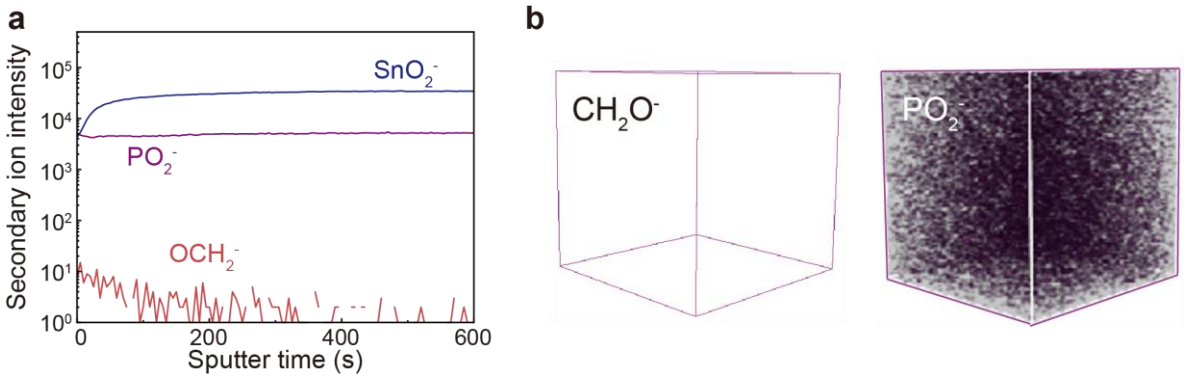

Fig. S33. *TOF-SIMS depth profiles (**a**) and corresponding 3D mapping (**b**) of a SnO_2 film deposited using DMPA additive without annealing.*

3) To understand why DMPA does not incorporate into the film despite being present in solution, we performed DFT calculations comparing the binding affinity of DMPA and SA ligands with Sn^{2+} (**Fig. S34**). The ester group ($-PO(OCH_3)_2$) of DMPA exhibited substantially weaker binding to Sn^{2+} than the sulfonic acid head group of SA. Moreover, even if the -COOH group of DMPA were to bind to Sn, the ester tail group lacks the ability to generate a negatively charged nanoparticle surface, a prerequisite for electrostatic adsorption onto the FTO substrate, as established in **Supplementary Note 3**. Consequently, the formation of a DMPA-capped SnO_2 layer is thermodynamically and kinetically unfavorable under our deposition conditions.

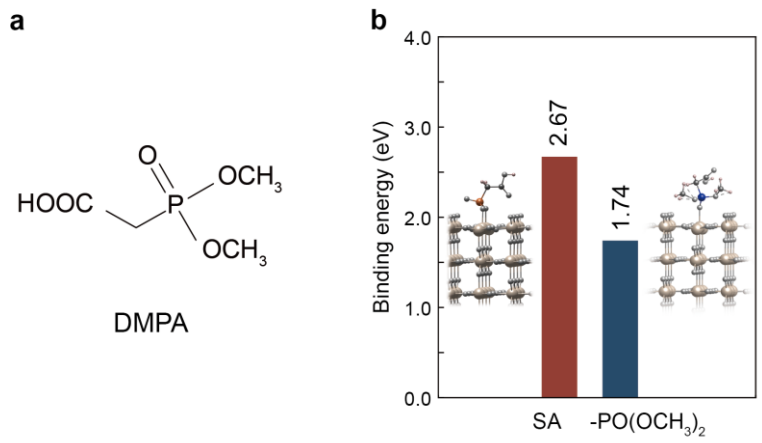

Fig. S34. *(**a**) Molecular structure of DMPA. (**b**) Calculated binding energy of SA and -PO(OCH₃)₂ group from DMPA ligands on SnO_2 surfaces.*

In summary, our combined experimental and theoretical analyses established that: DMPA undergoes controlled partial hydrolysis in the acidic CBD solution, serving as a slow-release source of PA ligands; the as-deposited ETL contains only PA-capped SnO_2, with no detectable DMPA incorporation, as confirmed by TOF-SIMS; and DFT calculations showed that DMPA's weak binding to Sn^{2+} and its inability to facilitate electrostatic adsorption preclude its participation in the film architecture. Therefore, the final ETL structure is unequivocally the SA-SnO_2 (n^+)/PA-SnO_2 (n) graded architecture, consistent with the design of our LCB strategy. We have incorporated these findings into the revised manuscript and supporting information to clarify the underlying chemistry.

Action: We have confirmed by real-time ^{31}P-NMR analysis that DMPA undergoes only partial hydrolysis during the CBD process. Moreover, TOF-SIMS measurements on as-deposited films (prior to annealing at 170 °C) and DFT calculations collectively demonstrated that the resulting graded film adopts an SA-SnO_2/PA-SnO_2 configuration, rather than an SA-SnO_2/DMPA-SnO_2 structure. These data were provided in **Supplementary Figs. 24-25**, with detailed discussions in **Supplementary Note 6** (**Pages 24-25**) and in the revised manuscript (**Line 202**, **Page 12**; **Line 252**, **Page 14**).

Comment 7. Is it possible to generate a graded structure by gradually introducing PA ligands into a solution that already contains SA ligands at an intermediate stage during a 4-hour chemical bath deposition process?

Response: We thank the reviewer for this constructive suggestion. To address whether a graded structure can be generated by introducing PA ligands at an intermediate stage of the deposition process (denoted as IPA strategy), we have performed additional experiments. We

have now confirmed that introducing PA ligands at an intermediate stage of the CBD process can construct a graded SnO_2 ETL, but this approach was insufficient for high-performance PSCs due to compromised film morphology and lateral inhomogeneity. Detailed experiments and discussion were provided below.

1) We continuously introduced PA ligands into the deposition solution at an intermediate stage during the 4 h CBD process. TOF-SIMS analysis of the resulting film (IPA-SnO_2) revealed a clear vertical gradient: the SO_3^- signal (representing SA ligands) progressively decreased from the FTO side toward the surface, while the PO_2^- signal (representing PA ligands) exhibited a complementary increase (**Fig. S35**). Accordingly, this confirmed that the IPA strategy is indeed capable of constructing a graded SnO_2 ETL.

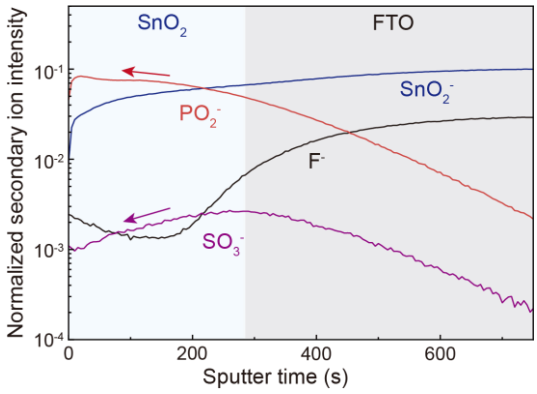

Fig. S35. *TOF-SIMS depth profiles of PO_2^- from PA and SO_3^- from SA in IPA-SnO_2 film.*

2) Despite achieving a ligand gradient, the IPA approach introduced two critical issues that undermine device performance. First, the continuous introduction of PA ligands during deposition led to severe particle aggregation, resulting in a rough and inhomogeneous film morphology (**Fig. S36a**). Second, TOF-SIMS mapping revealed pronounced in-plane heterogeneity of the PO_2^- distribution (**Fig. S36b**), indicating that the PA ligands were not uniformly incorporated across the substrate. These morphological and compositional inhomogeneities translate directly into degraded photovoltaic performance: devices fabricated with the IPA-SnO_2 ETL exhibited a PCE (reverse scanning, 26.40%) loss of up to 1.24% compared to the LCB-SnO_2 counterparts (reverse scanning, 27.64%) (**Fig. S37**).

In summary, while a graded SnO_2 ETL can indeed be constructed by introducing PA ligands at an intermediate stage, this approach suffered from compromised film morphology and lateral ligand inhomogeneity, which collectively limited its effectiveness for high-efficiency n-i-p perovskite solar cells. In contrast, our ligand-competitive binding (LCB) strategy achieved a clean vertical gradient without disrupting the uniform nanoparticle assembly, underscoring its superiority in balancing gradient formation with film quality.

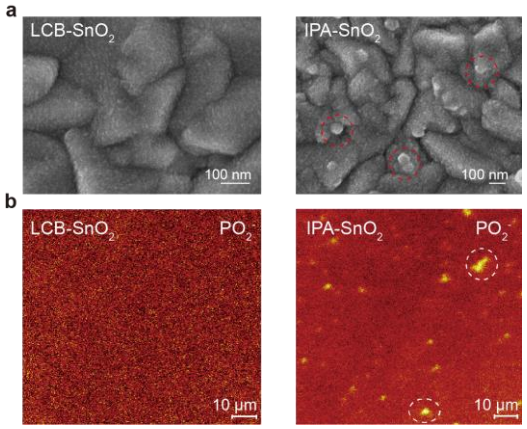

Fig. S36 *SEM images (**a**) and TOF-SIMS maps of PO_2^- (**b**) for LCB-SnO_2 film and IPA-SnO_2 film, respectively.*

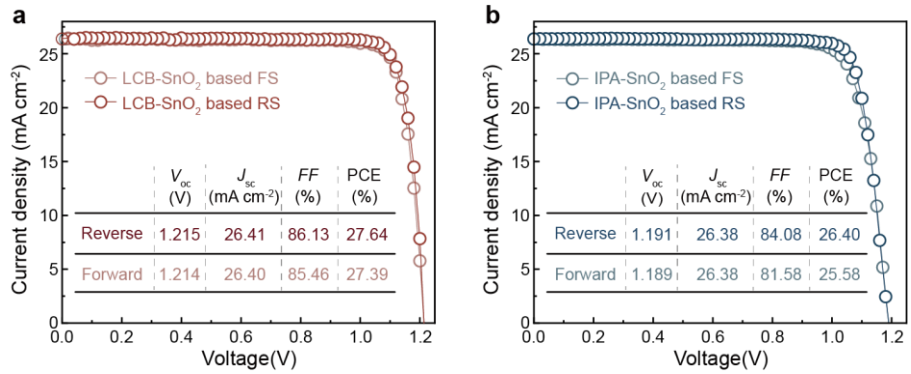

Fig. S37 *J-V curves for n-i-p devices based on LCB-SnO_2 ETL (**a**) and IPA-SnO_2 ETL (**b**).*

Action: We have now confirmed that introducing PA ligands at an intermediate stage of the CBD process can construct a graded SnO_2 ETL, but this approach was insufficient for high-performance PSCs due to compromised film morphology and lateral inhomogeneity. The corresponding analyses, including depth profiles and in-plane TOF-SIMS, and SEM characterization have been provided in the revised supporting information (**Supplementary Figs. 48-49**). The detailed discussion has been added in **Supplementary Note 10** (**Page 42**) and in the revised manuscript (**Line 322**, **Page 18**).

Comment 8. In the PCE certification report (Supplementary Fig. 23), the discrepancy in *FF* between the forward and reverse *J-V* scans (80.79% vs 86.48%) suggests pronounced hysteresis. Could this originate from residual ligands in the graded SnO_2 layer, or from other factors?

Response: We thank the reviewer for this important observation regarding the hysteresis behavior in the certified *J-V* scans. Through additional comparative measurements and analysis, we have now confirmed that the hysteresis did not originate from residual ligands in the graded

SnO_2 ETL, but rather reflects the well-documented measurement-protocol dependence of mixed ionic-electronic perovskite devices. As well known, steady-state efficiency is the accepted benchmark for reliable performance. Accordingly, the steady-state power output of 27.17% which represents the highest reported efficiency for n-i-p perovskite solar cells to date, providing a more reliable assessment of device performance. The detailed experiments and discussion were provided below.

1) Perovskite solar cells are mixed ionic-electronic conductors, in which ion migration is readily activated under applied bias. As a result, *J-V* hysteresis is known to be highly sensitive to measurement parameters, particularly scan rate, delay time, and voltage step, rather than solely reflecting bulk or interfacial defects (*Nat. Commun.* 2024, **15**, 9647; *Joule* 2018, **2**, 788-798; *Energy Environ. Sci.* 2015, **8**, 995-1004). This behavior is inherent to the perovskite absorber itself and does not necessarily indicate a deficiency in the charge transport layers.

2) To directly test whether the graded SnO_2 ETL contributes to hysteresis, we performed *J-V* measurements under varying scan parameters. As shown in **Fig. S38a**, when optimized conditions were employed, scan rate of 50 mV s^{-1}, delay time of 200 ms, and voltage step of 10 mV, the forward and reverse *J-V* curves became nearly hysteresis-free (**Extended Data Fig. 2b** in the manuscript). This demonstrated that the hysteresis observed in the certified report (**Supplementary Fig. 23**) primarily arose from the specific measurement parameters used during certification, rather than from residual ligands in the SnO_2 ETL. If the ligands were the root cause, the hysteresis would persist regardless of scan conditions. Hence, the observed hysteresis was primarily governed by measurement conditions.

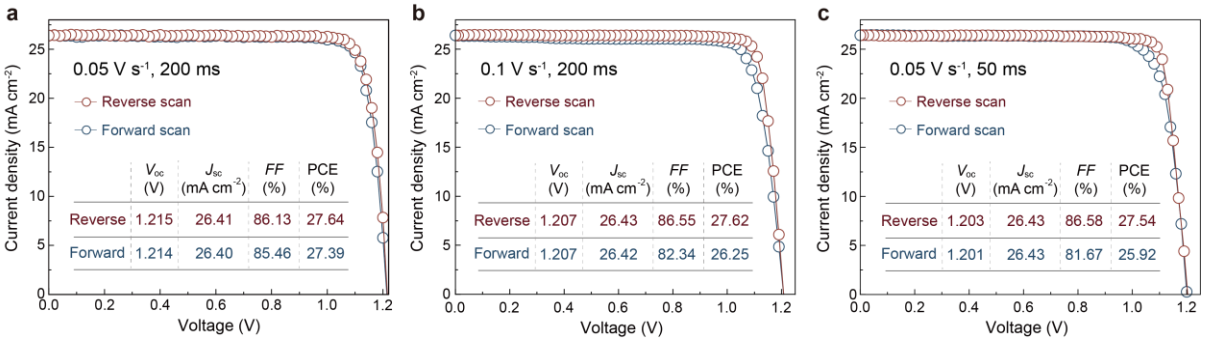

Fig. S38 *J-V curves for n-i-p devices measured under different conditions;* ***(a)*** *scan rate of 0.05 V* s^{-1} *with a delay time of 200 ms;* ***(b)*** *0.1 V* s^{-1} *with a delay time of 200 ms;* ***(c)*** *0.05 V* s^{-1} *with a delay time of 50 ms.*

3) Given the protocol-sensitive nature of *J-V* scans in perovskite devices, the photovoltaic community widely considers the steady-state power output, measured at the maximum power point under continuous illumination, as the most reliable indicator of actual device performance. As well known, **steady-state efficiency is the accepted benchmark for reliable performance**.

In this work, the certified steady-state efficiency of 27.17% (**Fig. S39**) not only confirmed the accuracy of the reported efficiency but also established a new record for n-i-p perovskite solar cells. Accordingly, this steady-state value is the key metric that substantiates the significance of our LCB-SnO_2 strategy.

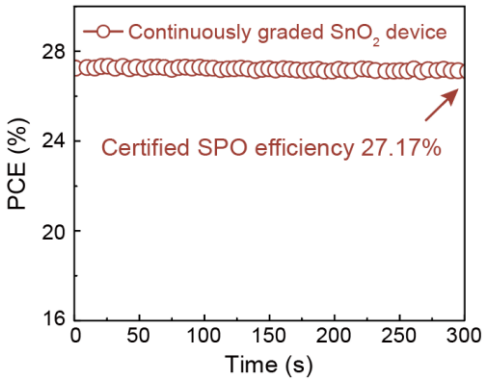

Fig. S39 *Certified steady-state PCE of continuously graded-doped SnO_2 based device after 300 s MPP tracking.*

In summary, the hysteresis observed in the certified *J-V* scans reflects the measurement-protocol dependence intrinsic to mixed ionic-electronic perovskite absorbers, rather than any inherent issue with the graded SnO_2 ETL. The near-hysteresis-free curves can be obtained under optimized conditions, further support this conclusion. Critically, the certified steady-state efficiency of 27.17% provides an unambiguous and reproducible demonstration of the superior device performance enabled by our graded SnO_2 architecture.

Action: We have now verified that the discrepancy in *FF* between forward and reverse scans (80.79% vs 86.48%) mainly originates from the pre-set scanning parameters. In particular, nearly hysteresis-free forward and reverse *J-V* curves were obtained using a scan rate of 50 mV s^{-1}, a delay time of 200 ms, and a voltage step of 10 mV. Related detailed discussion was provided in the revised manuscript (**Line 487**, **Page 28**).

Comment 9. It would be helpful for the authors to provide PL results to confirm the 1.51 eV bandgap of the perovskite, thereby strengthening the basis for the reported V_{oc} loss of 295 mV.

Response: We thank the reviewer for this constructive suggestion. To provide a more rigorous confirmation of the perovskite bandgap and thereby strengthen the basis for the reported V_{oc} loss, we have performed additional photoluminescence (PL) measurements alongside high-resolution external quantum efficiency (EQE) characterization, we have now confirmed that the perovskite bandgap is indeed 1.51 eV. The detailed experiments and analysis are provided below.

As shown in **Fig. S40a**, the PL emission peak of the perovskite absorber was located at ~822 nm. This value is consistent with the absorption edge extracted from the differential high-resolution EQE spectrum (step size of 1 nm), which appeared at ~820 nm (**Fig. S40b**). The excellent agreement between the PL peak position and the EQE-derived band edge, both measured independently, provided robust evidence that the perovskite bandgap is indeed 1.51 eV. Accordingly, the bandgap of 1.51 eV served as the critical reference for quantifying the V_{oc} loss in our devices, supporting the reported V_{oc} loss of 295 mV.

In summary, the combined PL and high-resolution EQE measurements consistently confirm a bandgap of 1.51 eV for the perovskite active layer, providing a reliable foundation for the reported V_{oc} loss of 295 mV. These data have been incorporated into the revised supporting information, and the corresponding discussion has been updated in the main text.

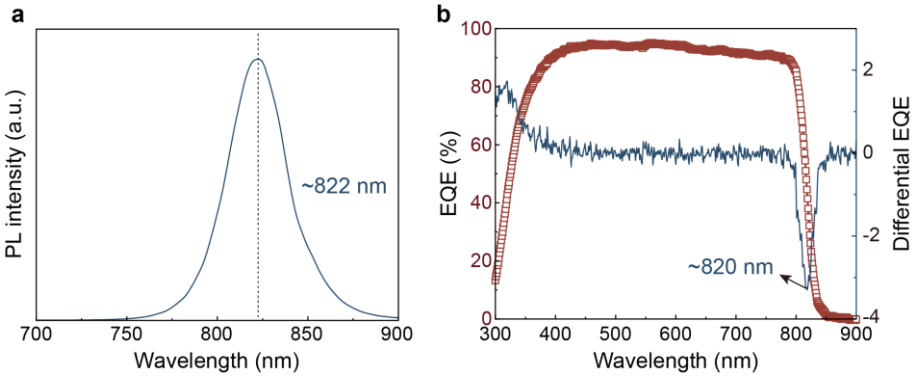

Fig. S40. *PL spectrum for perovskite absorber* ***(a)*** *and high-resolution EQE spectrum for PSCs* ***(b)****.*

Action: We have now provided additional PL spectrum of perovskite in **Supplementary Fig. 4**, and have updated the high-resolution EQE measurement in **Fig. 4c** in the revised manuscript. Related detailed discussion was provided in the revised manuscript (**Line 316**, **Page 18**).

Comment 10. Although the device performance for n-i-p perovskite solar cells is impressive, but thermal stability and thermal-recycling assessments are needed to be done in the revised manuscript.

Response: We thank the reviewer for this valuable suggestion. To comprehensively assess the thermal stability of devices based on the continuously graded SnO_2 ETL, we have now performed both damp-heat testing under the ISOS-D-3 protocol (85 °C and 85% RH) and thermal cycling testing following the IEC 61215:2021 standard (between -40 °C and 85 °C). The results, summarized below, demonstrated the excellent robustness of the graded SnO_2 architecture.

To accurately evaluate the stability of the SnO_2 ETL without interference from potential degradation of the hole transport layer, we replaced the conventional Spiro-OMeTAD with poly[bis(4-phenyl)(2,4,6-trimethylphenyl)amine] (PTAA), which exhibits superior thermal stability (*Nat. Energy* 2025, **10**, 774; *Science* 2022, **377**, 531 et al.). All devices were encapsulated with a UV-curable resin and cover glass prior to testing, ensuring that the observed degradation reflects intrinsic material stability rather than environmental ingress.

Encapsulated devices were subjected to continuous exposure at 85 °C and 85% relative humidity. As shown in **Fig. S41**, the devices retained 90% of their initial efficiency after 956 h of damp-heat stress. This level of stability was comparable to the best reported results for n-i-p perovskite solar cells (**Table 6**), confirming that the graded SnO_2 ETL maintains its functionality under harsh humid and thermal conditions.

To evaluate the resilience of the device stack against repeated thermal stress, we performed thermal cycling between -40 °C and 85 °C for 200 cycles. As shown in **Fig. S42**, the devices retained 88% of their initial efficiency after 200 cycles. This performance was consistent with state-of-the-art photovoltaic devices (**Table 7**) and demonstrated the mechanical and interfacial integrity of the graded SnO_2 structure under temperature cycling.

In summary, the graded SnO_2 ETL endows the device with excellent thermal stability, as evidenced by 90% efficiency retention after 956 h under damp-heat conditions and 88% retention after 200 thermal cycles. These results, together with the stability data presented earlier in the manuscript, collectively underscored the robustness of our LCB-SnO_2 architecture and its suitability for practical applications.

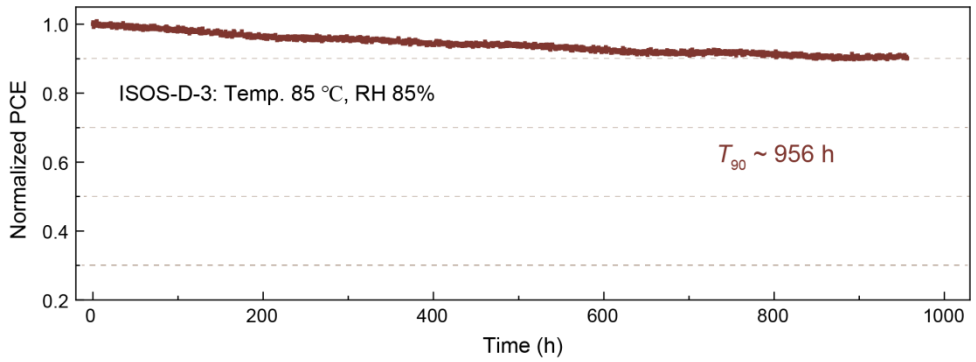

Fig. S41. *Damp-heat stability of the continuously graded-doped SnO_2-based encapsulated PSCs under ISOS-D-3 protocols (85 ℃, 85% relative humidity).*

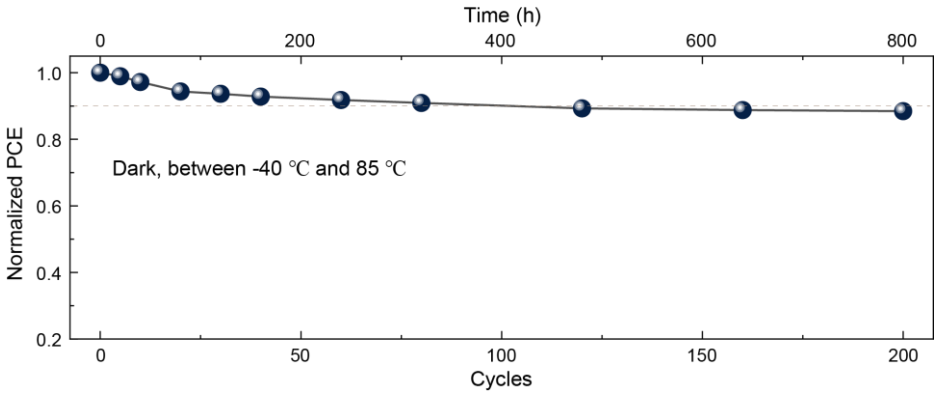

Fig. S42. *Thermal-cycling stability between -40 °C and 85 °C of the continuously graded-doped SnO_2-based encapsulated PSCs.*

Table 6. Summary of the reported operating stability of n-i-p PSCs under damp-heat conditions (ISOS-D-3 protocol).

ISOS protocol	Relative Humidity	Temperature	Lifetime	Ref.
ISOS-D-3	**~85%**	**85 °C**	**T_{90} = 956 h**	**This work**
ISOS-D-3	~85%	85 °C	T_{86} = 900 h	*Nat. Energy* 2025, 10, 774
ISOS-D-3	~85%	85 °C	T_{92} = 600 h	*Science* 2024, 384, 878

Table 7. Summary of the reported operating stability of n-i-p PSCs under thermal-cycling conditions.

Temperature	Cycles	PCE retention (%)	Ref.
-40~85 °C	**200**	**T_{88} = 800 h**	**This work**
-40~85 °C	200	T_{80} > 1200 h	*Science* 2024, 384, 878
-40~85 °C	200	90%	*Angew. Chem. Int. Ed.* 2025, 64, e202421063

Action: We have now provided additional operational stability data for devices using PTAA as HTL, under ISOS-D-3 damp-heat conditions (85 °C and 85% RH) and thermal cycling between -40 °C and 85 °C in **Supplementary Figs. 51-52** and **Supplementary Tables 6-7**. The devices retained ~90% of their initial efficiency after 956 h of continuous operation and maintained 88% of the initial efficiency after 200 thermal cycles, confirming the robustness of the graded SnO_2 structure. The related discussion has been incorporated into the revised manuscript (**Line 337**, **Page 19**) and **Supplementary Note 12**.

Comment 11. I appreciate the SI writing style that combines the Supplementary Notes and Supplementary Figures, which greatly facilitates understanding. For even smoother reading, it may be helpful if the authors could consider aligning the numbering of figures and supplementary figures with the order of their appearance in the corresponding text.

Response: We thank the reviewer for the positive feedback on the structure of our supporting information. To further enhance readability, we have now carefully aligned the numbering of all figures and supplementary figures with the order of their first appearance in the main text and supplementary notes.

For instance, **Supplementary Fig. 10** in the original version has been renumbered as **Supplementary Fig. 8** to match its first citation (**Line 109**, **Page 6**). Additionally, the AIMD data previously presented in **Supplementary Fig. 20** have been repositioned to appear before the section discussing controlled hydrolysis, improving the logical flow. All newly added or revised figures and notes have been systematically reordered to follow the sequence in which they are discussed. These adjustments ensure a more coherent and reader-friendly presentation throughout the supporting information.

Action: We have now carefully aligned the numbering of all figures and supplementary figures with the order of their first appearance in the corresponding text.

Comment 12. Minor mistakes:1. Line 250, Page 14: A Chinese comma symbol (“，”) is used.

Response: Sorry for the typo. We have now revised the *Chinese comma symbol* (“，”) to *Times New Roman* “,” and rechecked the manuscript thoroughly to avoid any grammar or typo errors.

Action: We have now revised the *Chinese comma symbol* (“，”) to *Times New Roman* “,” in the revised manuscript (**Line 273**, **Page 15**).

Referee #3:

A. In this report, the authors describe the utilization of a graded SnO_2 bandgap that achieves a near 10% enhancement in the efficiency of a perovskite solar cell. The authors identify a defect within the SnO_2 electron transport layer that hinders charge transfer and directly impacts the voltage and FF. Through simulations, they attribute this to oxygen vacancies that act as shallow donors. The authors surmise that this is due to the CBD deposition of the SnO_2 nanoparticles and propose that this can be resolved using a straightforward ligand strategy. However, to accomplish this, they employ a rather unique chemical strategy to manage the ligand. As a result, they are able to utilize the CBD process to create a graded bandgap. With this in place, they are able to demonstrate an improved efficiency for a device on a non-uniform surface. This paper is well-written and the narrative manages the reader's interest and builds a solid story. From the scientific merits of the work, it is solid.

B. The proposed ligands and use of ligands to achieve highly uniform results with SnO_2 have been studied before, as described by the authors. However, the use of the dual ligand strategy to achieve a graded bandgap using the CBD strategy is novel.

C. The data quality and the utilization of experiments and simulations to identify the issues associated with the buried interface, along with the validation of the proposed solution's effectiveness, are present.

D. The authors employ a sufficient number of devices to conduct a robust statistical analysis.

E. The conclusions are supported by the data.

F. The primary concern from this reviewer's perspective is the need for an improved ETL for a non-uniform surface and of course how this process is expanded for high throughput production.

1- The authors' motivation in the introduction is that the utilization of textured surfaces for light management has enhanced the power conversion efficiency (PCE) of photovoltaic cells. Textured surfaces are often incorporated into silicon solar cells and contribute to improved PCE. Consequently, the development of chemistries and processes aimed at achieving higher efficiencies is driven by the tandem architecture, which favors the p-i-n structure.

a. Thus it would be helpful if the authors address this issue, ie, can this process be adapted to perovskite/tandems or what is the opportunity for these devices.

b. On line 82 page 4, the authors describe the fabrication of SnO_2 on a textured FTO, but do not mention the RMS of the textured FTO. The amount texture as seen in Fig 2g, and SI 16 shows a pyramid like structure about 100-200 nm tall. And these do not seem to be distributed over the larger area. So, the RMS is probably on the order of 10's of nm. In contrast a textured surface for a silicon solar cell uses pyramids of several microns and optimized texturing for perovskite/silicon tandems the pyramids are ~0.5 microns. Thus, the authors are encouraged to put a bit more context on the texturing.

c. It would also be helpful to the reader if the authors discussed the importance of the RMS values on their process. Is there a point that the CBD and/or grade bandgap breaks down.

2- The chemical bath deposition process is a scalable process and can result in large area uniform films (1 m^2), and has been demonstrated for CIGS devices. However, the reality is that the process in inherently slow, as is detailed within this manuscript. Therefore it would aid the reader if the authors would provide a prospective of the utility of the proposed chemistry/process.

G. References are appropriate.

H. The manuscript is well-written, and the story has a logical narrative. The authors are encouraged to provide context for the scientific discussion in the broader implications of this study, as outlined above.

Response: We really appreciate the reviewer's encouraging comments. By carrying out additional experiments and simulations, we have now fully addressed the concerns raised by the reviewer. We believe the quality of the manuscript have been substantially reinforced now due to your great helps.

Comment 1. Thus it would be helpful if the authors address this issue, ie, can this process be adapted to perovskite/tandems or what is the opportunity for these devices.

Response: We thank the reviewer for the insightful comment. Through additional cross-sectional SEM and EDS analyses, we have now verified that the CBD SnO_2 deposition is incompatible with the fabrication of high-performance perovskite/silicon tandem solar cells, as the strongly acidic aqueous solution corrodes and partially dissolves the ultrathin transparent conductive oxide (TCO) layer. In contrast, devices fabricated using our graded CBD SnO_2 approach, including large-area cells (1 cm^2) and mini-modules (5 × 5 cm^2), exhibited power conversion efficiencies of 25.79% and 23.33%, respectively. These values were comparable to

the state-of-the-art cells reported to date, highlighting the scalability and practical potential of our method.

Details of the experiments and discussion were provided below:

1) Consistent with previous reports (*Nature* 2021, **590**, 587-593; *Nat. Energy* 2025, **10**, 774-784, et al.), the CBD SnO_2 ETL process must be conducted under strongly acidic conditions (pH = 1-3) to suppress the rapid hydrolysis of Sn^{2+} (as described in **Equation 5**), which is essential for achieving uniform deposition.

$$Sn^{2+} + H_2O \rightleftharpoons Sn(OH)^+ + H^+ \quad 5$$

We therefore investigated the stability of the bottom-cell substrate in perovskite/silicon tandem devices under such acidic conditions. As illustrated in **Fig. S43**, the state-of-the-art perovskite/silicon tandems typically employ an ultrathin transparent conductive oxide (TCO) recombination layer to electrically connect the two subcells prior to the deposition of the perovskite top cell ETL. In high-efficiency devices, this recombination layer is typically based on Sn-doped In_2O_3 (ITO), as demonstrated in recent studies (*Nature* 2026, **649**, 59-64; *Science* 2025, **390**, eadx1745; *Joule* 2026, **10**, 102237; *Nat. Commun.* 2025, **16**, 40, et. al.).

[Figure Redacted]

Fig. S43. *Schematic structure of perovskite/silicon tandem solar cells.*

However, as shown in **Fig. S44a**, the sputtered ITO layer exhibited visibly corrosion and partial dissolution after CBD deposition. Cross-sectional SEM further revealed that the original Si/ITO substrate had transformed into a smooth Si surface (**Fig. S44b**), indicating severe etching of the TCO layer. Corresponding energy-dispersive X-ray spectroscopy (EDS) analyses (**Figs. S44c-f**) showed that the indium (In) atomic ratio in both cross-sectional and planar samples fell to undetectable levels (0 wt%) after CBD process, confirming the complete removal of the ITO layer.

These results unambiguously demonstrated that the strongly acidic CBD process is incompatible with the fabrication of high-performance perovskite/silicon tandem cells, as it severely damages the ultrathin TCO recombination layer. This finding was consistent with earlier reports showing that acidic environments can corrode ITO or IZO recombination layers (*Angew. Chem. Int. Ed.* 2024, **63**, e202403824; *eScience* 2024, **4**, 100241).

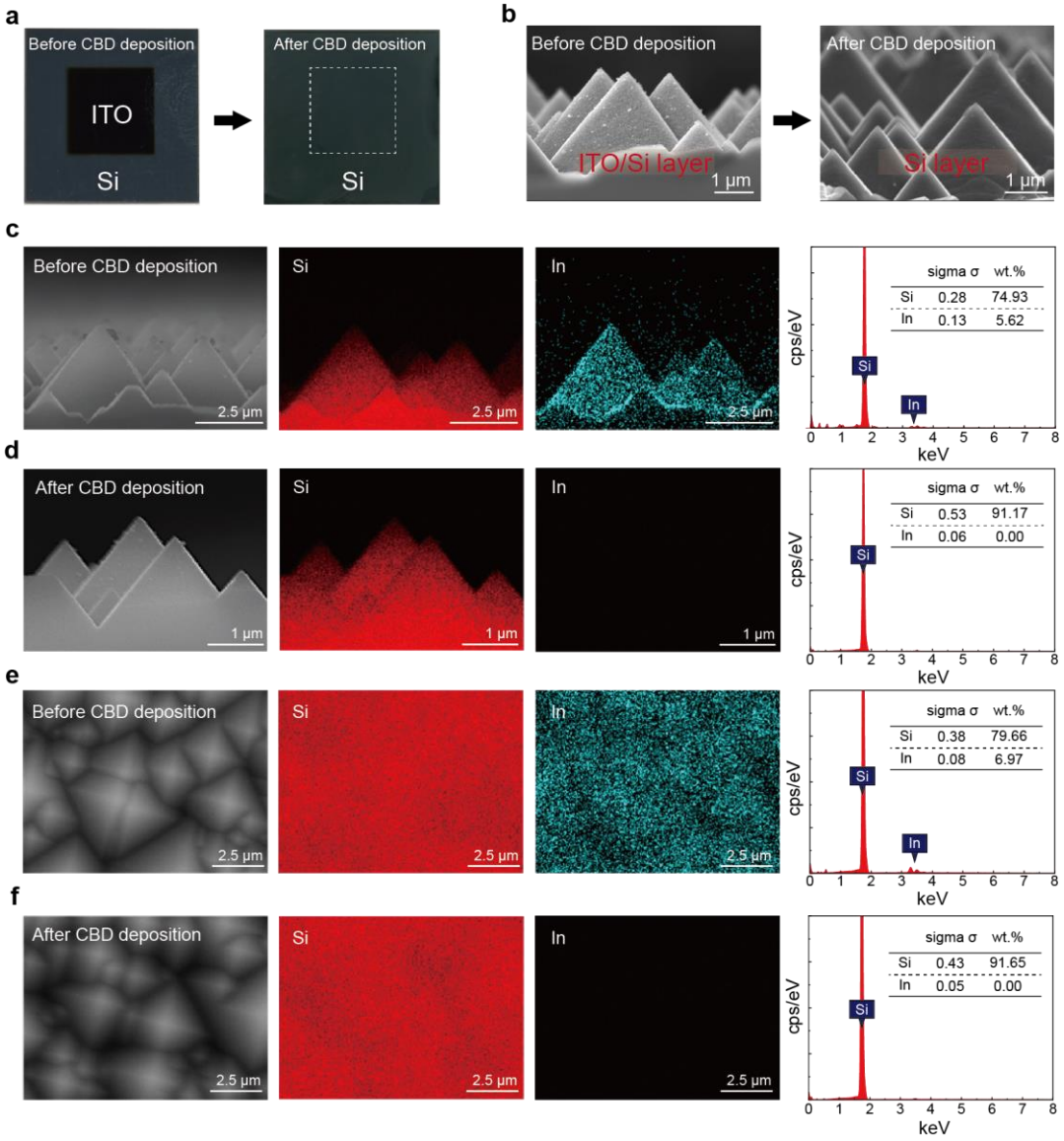

Fig. S44. *(**a**) Photographs of Si/ITO substrate before (left) and after (right) CBD deposition. (**b**) Cross-sectional SEM images of the Si/ITO substrate before (left) and after (right) CBD deposition. EDS spectra of cross-sectional (**c**, **d**) and planar (**e**, **f**) Si/ITO substrates before and after CBD deposition.*

2) Nevertheless, the CBD process offers intrinsic advantages for the fabrication of large-area modules, including scalability independent of substrate size and geometry, conformal coverage, and low cost. Owing to these merits, it has emerged as a promising approach for fabricating

high-quality SnO_2 ETLs and has been widely adopted in high-efficiency modules (*Nat. Energy* 2025, **10**, 774-784; *Nature* 2024, **633**, 359-364; *Science* 2024, **386**, 531-538, et al.).

In the revised manuscript, by employing the continuously graded-doped CBD SnO_2 ETL, we have now reported high-performance large-area PSCs, with power conversion efficiencies of 25.79% for a 1 cm^2 device and 23.33% for a 5 × 5 cm^2 module (**Fig. S45**). Particularly, these values are comparable to the state-of-the-art cells reported to date (*Nat. Photon.* 2026, **20**, 55-62; *Nat. Energy* 2025, **10**, 774), highlighting the scalability and practical potential of our approach. Detailed procedures for the fabrication of the modules were provided in the Methods section in the revised manuscript (**Line 480**, **Page 27**).

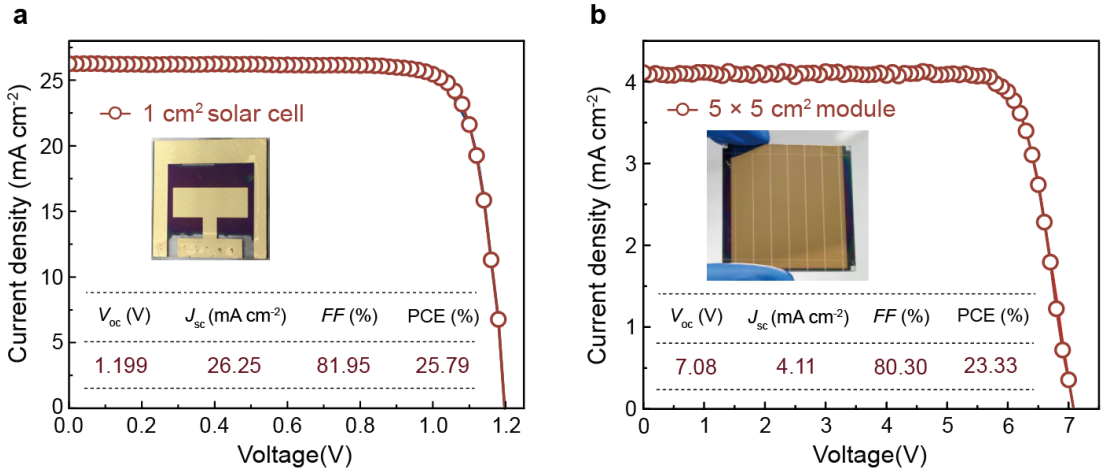

Fig. S45. *J-V curves of continuously graded-doped SnO_2 based PSCs for 1 cm^2 device (**a**) and 5 × 5 cm^2 module (**b**), respectively.*

Therefore, we envisioned that the true potential of the CBD process will be realized in high-performance single-junction solar cells, with promising applications in building-integrated photovoltaics (BIPV) and flexible photovoltaics, where its scalability and low-temperature processing offer distinct advantages for industrial adoption (*Nat. Energy* 2025, **10**, 774-784; *Joule* 2025, **9**, 102056; *Adv. Mater.* 2024, **36**, 2307357).

Action: We have now verified that the CBD SnO_2 process is incompatible with the fabrication of high-performance perovskite/silicon tandem cells, as the strongly acidic conditions severely damage the ultrathin TCO recombination layer. In contrast, we identified that the primary opportunity for this method lies in high-performance single-junction applications, particularly for large-area building-integrated photovoltaics (BIPV) and flexible photovoltaic. To support this, we have now reported efficiencies of 25.79% for 1 cm^2 device, and 23.33% for 5 × 5 cm^2 module using our graded CBD SnO_2, as shown in **Extended Data Fig. 2**. Detailed fabrication procedures for the solar modules were provided in the Methods section **(Line 478**, **Page 27)**,

and further discussion was available in the revised manuscript (**Line 41**, **Page 2**; **Line 82**, **Page 4**; **Line 331**, **Page 19**).

Comment 2. On line 82 page 4, the authors describe the fabrication of SnO_2 on a textured FTO, but do not mention the RMS of the textured FTO. The amount texture as seen in Fig 2g, and SI 16 shows a pyramid like structure about 100-200 nm tall. And these do not seem to be distributed over the larger area. So, the RMS is probably on the order of 10's of nm. In contrast a textured surface for a silicon solar cell uses pyramids of several microns and optimized texturing for perovskite/silicon tandems the pyramids are ~0.5 microns. Thus, the authors are encouraged to put a bit more context on the texturing.

Response: We thank the reviewer for the insightful comment. Through AFM measurement, we have now confirmed that the FTO substrate used in this work exhibited an RMS roughness of 43.9 nm, with pyramid feature maximum heights reaching approximately ~200 nm. Furthermore, we performed additional 3D FDTD simulations to elucidate the distinct design principles underlying light management in perovskite solar cells. We have now highlighted that the micron-scale texture in crystalline silicon cells is optimized for long-wavelength light trapping in a thick, indirect bandgap absorber, whereas the nanoscale features in perovskite devices prioritize efficient short-path absorption enhancement and are designed to remain compatible with the constraints of thin-film fabrication.

The detailed experiment and simulation analyses were as follows:

1) The surface morphology of the FTO substrate used in this work was characterized by AFM measurement. As presented in **Fig. S46**, we have now determined the substrate exhibited an RMS roughness of 43.9 nm, and featured pyramid-like textures with maximum heights of ~200 nm.

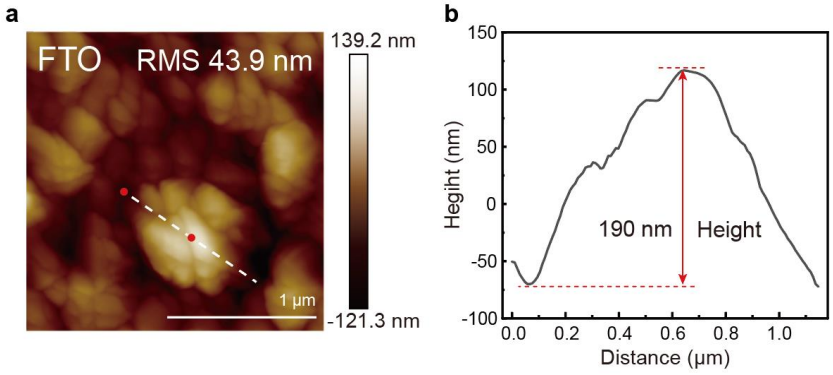

Fig. S46. *(**a**) AFM image of FTO substrate used in this work. (**b**) Height distribution profile along with the white dashed line region in Fig. 46a.*

2) We have now demonstrated that the optimal texture scale is intrinsically linked to the device architecture and absorber properties.

In silicon or perovskite/silicon tandem solar cells, the relatively low absorption coefficient of silicon, a consequence of its indirect bandgap, necessitates efficient light trapping. As a result, micron-scale pyramidal textures are typically employed. These structures operate in the geometric optics regime, where incident light undergoes multiple reflections and refraction into the high-refractive-index silicon bulk. The random facet orientations further scatter light into angles that satisfy total internal reflection, thereby significantly extending the optical path length, approaching the theoretical Lambertian limit of $4n^2$. Such strong light trapping is particularly critical for long-wavelength photons near the silicon bandgap (900-1100 nm), where the absorption coefficient is low and the absorption length can extend to hundreds of micrometers or even more. Given that industrial *c*-Si wafers are typically around 180 μm thick, multiple traversals of weakly absorbed photons are required for near-complete absorption. Micron-scale pyramids efficiently randomize ray directions, maximizing the probability of such extended optical paths while reducing front-surface reflectance.

In contrast, textured substrates employed in perovskite solar cells typically feature nanoscale structures on the order of 100 nm, operating in a different optical regime tailored to the distinct properties of perovskite absorbers. The absorbers are typically very thin (~500 - 800 nm), with much higher absorption coefficients across most of the visible spectrum, eliminating the need for geometric-optics-based multi-pass light trapping. Instead, nanoscale textures provide broadband, angle-insensitive anti-reflection through an effective medium effect, while avoiding the excessive surface recombination and processing incompatibilities that arise when larger textures are used in solution-based perovskite deposition (*Nature* 2023, **624**, 289-294; *Science* 2022, **375**, 302-306; *Light Sci. Appl*. 2026, **15**, 56; *Nanophotonics* 2021, **10**, 2023-2042). Therefore, the use of nanoscale texturing in our work is consistent with the optical and fabrication requirements of perovskite devices, whereas micron-scale pyramids are specifically optimized for light trapping in thick, indirect-bandgap silicon absorbers.

To quantitatively assess the optical impact of texture scale in perovskite solar cells (PSCs), we performed additional 3D FDTD optical simulations combined with APSYS software. As shown in **Fig. S47**, the presence of textured substrates indeed enhanced the corresponding photocurrent density (J_{sc}) of the devices. However, the simulations further revealed that when pyramid heights approach the microscale, comparable to those used in silicon photovoltaics, no significant photocurrent gain was observed in PSCs with absorber thicknesses on the order

of hundreds of nanometers. These results collectively demonstrated that nanoscale texturing is more suitable for single-junction perovskite solar cells, offering an optimal balance between optical performance and compatibility with thin-film device constraints.

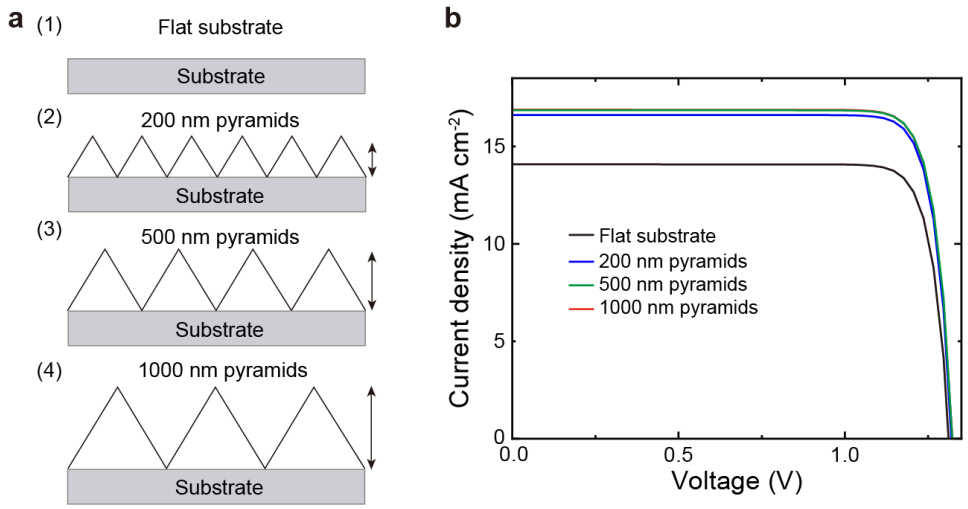

Fig. S47. *(**a**) Schematic illustrations of FTO substrates with different pyramids heights. (**b**) Simulated J-V curves of devices based on FTO substrates with varying pyramid heights.*

Action: We have now characterized the RMS roughness of the FTO substrate used in this work. As presented **Supplementary Fig. 27**, we verified the FTO exhibits an RMS roughness of 43.9 nm, and features pyramid-like textures with maximum heights of ~200 nm. To further elucidate the role of texture scale in perovskite solar cells, we performed additional 3D FDTD optical simulations (**Supplementary Fig. 30**). The results confirmed that nanoscale texturing is more suitable for single-junction perovskite devices. This distinction arises primarily from the direct bandgap nature of perovskites, which contrasts with the indirect bandgap of silicon and its corresponding requirement for micron-scale light trapping. Detailed analysis and discussion have been provided in **Supplementary Note 8** and in the revised manuscript (**Line 47**, **Page 3**), and the 3D FDTD optical simulation methodology was described in the **Methods** section of the revised manuscript of (**Line 493**, **Page 28**).

Comment 3. It would also be helpful to the reader if the authors discussed the importance of the RMS values on their process. Is there a point that the CBD and/or grade bandgap breaks down.

Response: We thank the reviewer for the insightful comment. To assess the influence of substrate roughness on our process, we have examined the conformality and graded-structure formation of the CBD SnO_2 layer on substrates with varying RMS roughness, including highly textured surfaces with pyramid heights up to ~3 μm. Across all tested substrates, we observed

no evidence of process breakdown; the CBD SnO_2 layer maintained excellent conformal coverage, and the continuously graded doping profile was successfully preserved. This robustness is attributed to the *quasi*-layer-by-layer nanoparticle assembly mode inherent to the CBD process, which enables uniform deposition even on complex textured surfaces. Additional cross-sectional HAADF-STEM and TOF-SIMS characterizations have now been provided to support these findings. These results demonstrated that our CBD approach is highly tolerant to substrate topography and suitable for integration with a wide range of device architectures.

Details of the experiments and discussion were provided below:

1) To investigate the influence of substrate RMS roughness on the CBD deposition process, we selected three substrates with distinctly different surface morphologies, as characterized by AFM measurements (**Fig. S48**): a low-texture FTO substrate (FTO-1, RMS = 12 nm, pyramids height ~60 nm), a moderately textured FTO substrate (FTO-2, RMS = 43.9 nm, pyramids height ~200 nm, used in this work), and a highly textured Si substrate (Si, RMS = 400 nm, pyramids height ~2 - 3 μm as confirmed by cross-sectional HAADF-STEM). SnO_2 ETLs were then deposited onto each of these substrates using the same CBD process.

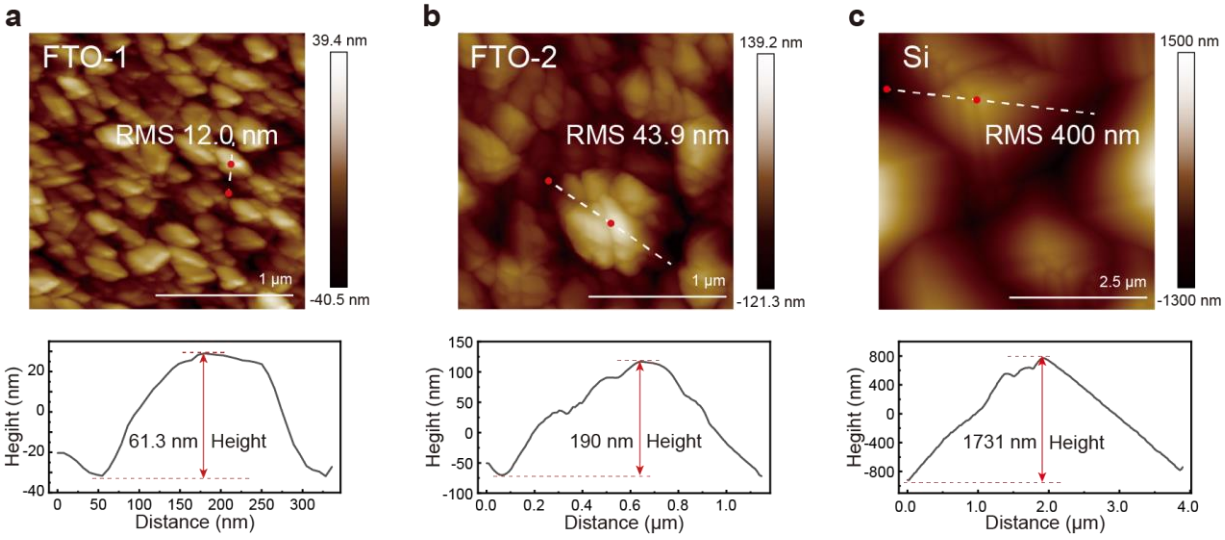

Fig. S48. *AFM images (left) and the corresponding height profiles (right) extracted along the white dashed line of FTO-1 (**a**), FTO-2 (**b**), Si (**c**) substrates, respectively.*

To assess whether conformal coverage can be achieved across substrates with markedly different surface textures, we performed cross-sectional HAADF-STEM measurements on the three representative samples. As shown in **Figs. S49** and **S50**, uniform and conformal SnO_2 ETLs were successfully deposited on all substrates, ranging from nanoscale FTO pyramids

(~50 - 200 nm) to micro-scale Si pyramids (~3 μm). These results confirmed the excellent conformality and broad substrate adaptability of the CBD process.

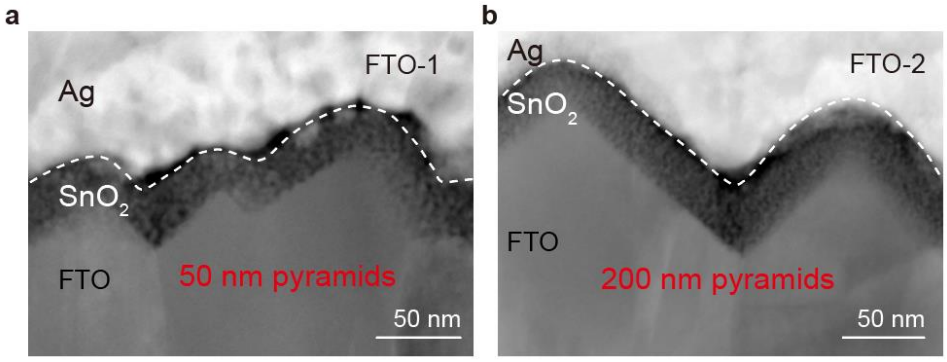

Fig. S49. *Cross-sectional HAADF-STEM images of CBD SnO_2 deposited on FTO-1 (**a**) and FTO-2 (**b**) substrates, respectively.*

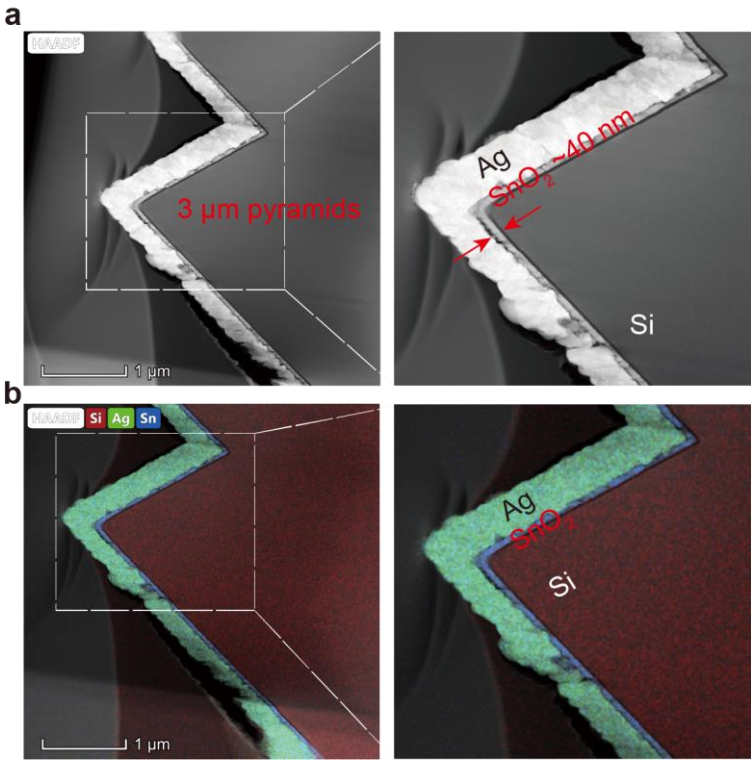

Fig. S50. *Cross-sectional HAADF-STEM images (**a**) and EDS maps (**b**) of CBD SnO_2 deposited on Si with 3 μm pyramids, the right images were enlarged pictures.*

2) To further examine whether RMS values affect the construction of the graded structure, we performed additional TOF-SIMS measurements on SnO_2 films deposited on the two representative substrates: low-texture FTO-1 and highly-textured Si substrate. As shown in **Fig. S51**, in both cases, the SO_3^- signal (representing SA ligands) progressively decreased from the bottom side toward SnO_2 interface, while the PO_2^- signal (representing PA ligands) showed a complementary increase. These results confirmed the successful construction of a graded

structure, consistent with the observation on the FTO-2 substrate used in our manuscript (**Fig. 2h** in the manuscript).

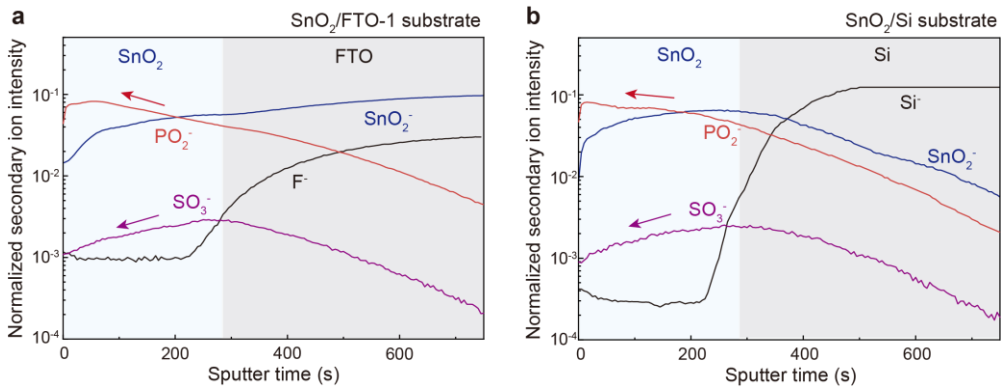

Fig. S51. *TOF-SIMS depth profiles of PO_2^- from PA and SO_3^- from SA for SnO_2 film deposited on FTO-1 substrate (**a**) and Si substrate (**b**).*

Collectively, these results demonstrated that the CBD SnO_2 process, which proceeds through the *quasi*-layer-by-layer assembly of 3-5 nm nanoparticles (**Line 116** in the manuscript), enables conformal and graded-structured deposition upon substrates with varying RMS roughness, exhibiting no observable breakdown limit even on highly textured surfaces.

Action: We have now confirmed that the CBD process exhibited no observable breakdown limit, enabling conformal and graded-structure deposition on substrates with arbitrary surface roughness. The corresponding cross-sectional HAADF-STEM images of SnO_2 films deposited on variously textured substrates have been provided in **Supplementary Figs. 28-29**, and corresponding TOF-SIMS depth profiles were shown in **Supplementary Fig. 31**. Detailed analysis and discussion were available in **Supplementary Note 8** and the revised manuscript (**Line 260**, **Page 14**).

Comment 4. The chemical bath deposition process is a scalable process and can result in large area uniform films (1 m^2), and has been demonstrated for CIGS devices. However, the reality is that the process in inherently slow, as is detailed within this manuscript. Therefore it would aid the reader if the authors would provide a prospective of the utility of the proposed chemistry/process.

Response: We thank the reviewer for raising this important point regarding the throughput of the CBD process. We acknowledge that, as detailed in our original manuscript, the deposition kinetics are relatively slow. In response, we have now optimized the controlled hydrolysis process to shorten the CBD deposition time to 1 hour, which is comparable to that of typical ALD and sputtering processes. Furthermore, we also offer a perspective on the utility of this

process based on three considerations. Details of the experiments and discussion were provided below.

1) We thank the reviewer for raising this important point regarding the throughput of the CBD process. To address this, we have now optimized the deposition conditions to reduce the processing time while preserving the graded structure of SnO_2 ETL.

The relatively slow deposition kinetics arises from the intrinsic nucleation and growth behavior of the system. Specifically, the reaction is initiated in a strongly acidic environment to suppress the rapid hydrolysis of Sn^{2+} (as described in **Equation 5**, previous response to Comment 1). Upon heating, the gradual decomposition of urea steadily increases the pH, thereby driving the reaction forward. As a result, the system undergoes a distinct "incubation period" before reaching the critical supersaturation—during which no film is deposited on the substrate. This behavior is consistent with the thickness-time profile shown in **Supplementary Fig. 9** (**Fig. S52a**), where negligible film growth was observed within the first ~1.5 h, followed by a rapid growth regime. Based on this understanding, we implemented a precursor dilution strategy by diluting the initial solution twelvefold. This approach effectively increased the initial pH and accelerated its rise, thereby promoting earlier nucleation and faster film growth. As a result, the deposition kinetics were significantly enhanced, shortening the total CBD time to 1 h, in line with previous reports (*Nat. Energy* 2025, **10**, 774; *Nature* 2023, **616**, 724; *Science* 2026, **391**, 6781), while yielding a ~25 nm thick film with a conformal morphology (**Fig. S52b**).

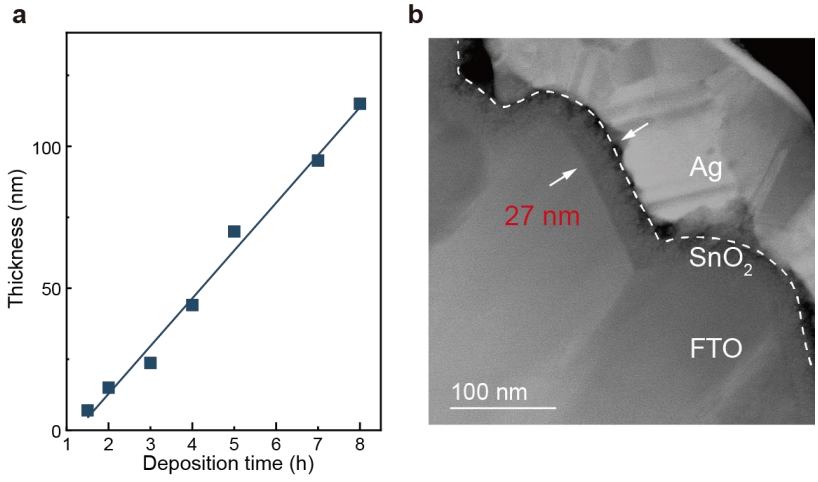

Fig. S52. ***(a)*** *SnO_2 films thickness versus deposition time profile.* ***(b)*** *Cross-sectional TEM image of SnO_2 with 1 h deposition.*

To preserve the continuously graded structure within the shortened 1 h deposition window, the initial DMPA concentration was re-optimized according to the hydrolysis kinetics equation, $[A] = [A]_0 \exp(-4.845 \times 10^{-6} t)$, where $[A]_0$ and $[A]$ represent the initial and time-dependent DMPA concentrations, respectively, yielding an optimal value of 8.411 mM to ensure a graded

release of PA ligands. To verify the resulting structure, additional TOF-SIMS depth profiling was conduct. As shown in **Fig. S53a**, the SnO_2 film retained a graded structure, with the SO_3^- signal progressively decreasing and the PO_2^- signal progressively increasing toward the SnO_2/perovskite interface. Consequently, under these optimized conditions, devices fabricated using this accelerated process achieved performance comparable to that reported in the original manuscript (**Fig. S53b**).

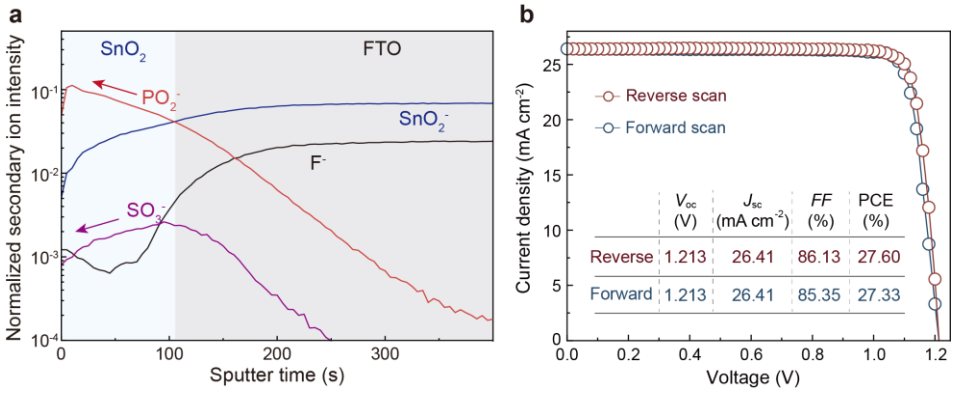

Fig. S53. *(**a**) TOF-SIMS depth profiles of PO_2^- from PA and SO_3^- from SA for SnO_2-1 h. (**b**) J-V curves of n-i-p PSCs based on SnO_2-1 h.*

2) We would like to offer a perspective on the utility of the CBD process based on following three considerations:

First, the trade-off between rate and functionality. The moderate deposition rate is intrinsically linked to the formation mechanism of the graded structure. This kinetic window enables the in-situ ligand exchange and self-assembly that yield the continuously graded SnO_2 ETL, a feature critical to achieve the high V_{oc} and *FF* reported in our large-area devices and modules. Such precise chemical tailoring is difficult to replicate with faster, non-equilibrium physical deposition techniques.

Second, scalability and cost-of-ownership. For industrial-scale production targeting substrates at the 1 m^2 level or beyond, the capital expenditure of vacuum-based systems escalates significantly. In contrast, CBD is an open-atmosphere, bath-based process that scales linearly with substrate size. When implemented in a batch or inline configuration, the effective throughput (substrates/hour) can meet manufacturing demands while maintaining excellent uniformity, as previously demonstrated in the CIGS industry.

Third, performance normalization. The ultimate utility of any process in photovoltaics is measured by its contribution to levelized cost of electricity. Our graded CBD SnO_2 process yields power conversion efficiencies of 25.79% for a 1 cm^2 device and 23.33% for a 5 × 5 cm^2

module (**Fig. S45**, previous response to Comment 1). The significant efficiency gain, enabled by the superior conformality and band alignment of the CBD-derived ETL, offsets the slightly longer deposition time, resulting in a favorable trade-off for high-value applications such as building-integrated photovoltaics and flexible modules.

Action: We thank the reviewer for raising this important point regarding the throughput and practical utility of the CBD process. To provide a comprehensive perspective, we have now discussed the scalability and industrial relevance of our approach in **Supplementary Note 11** (**Page 47**). Detailed analysis and discussion have been provided in **Supplementary Fig. 32** and in the revised manuscript (**Line 262**, **Page 14**; **Line 331**, **Page 19**).